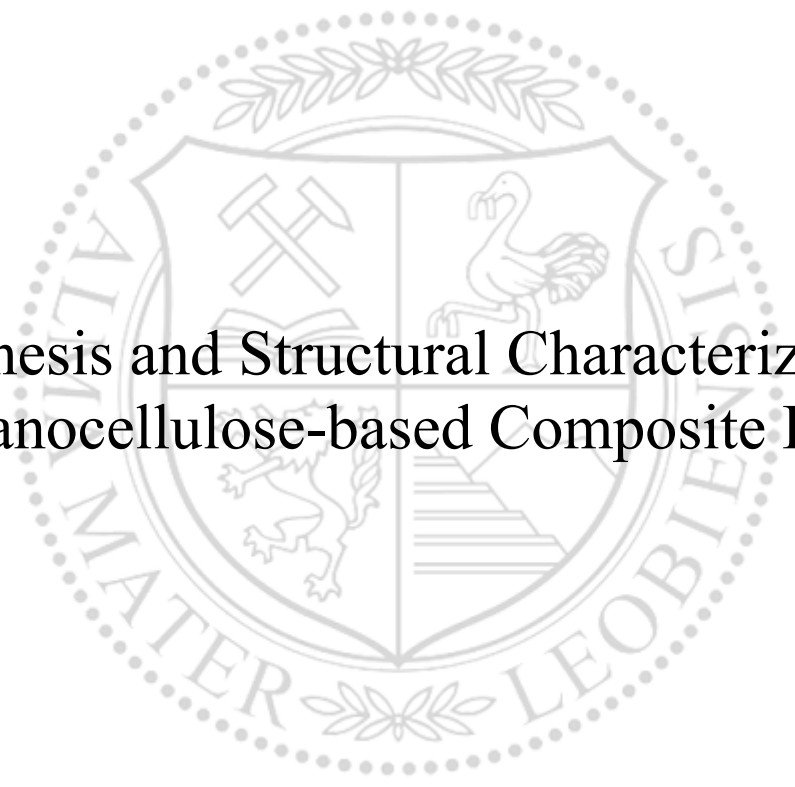Chair of Physics

Master's Thesis

Synthesis and Structural Characterization of Nanocellulose-based Composite Films

Hanno Lorenz Holzinger, BSc

September 2020

Acknowledgements

I would like to begin by thanking everyone that has supported me over the entire duration of my studies – first and foremost my family and my girlfriend who have been with me through all the ups and downs, that have lent me an ear whenever I needed it and that reassured me when I was doubting myself. I would not know what I would have done without you.

I would like to express my deepest appreciation to my supervisor Dr. Gerhard Popovski for his support and guidance while writing this thesis as well as his never-ending contagious enthusiasm and positive attitude that motivated me throughout the whole process and beyond when for example working together in the laboratory courses in Physics. I would also like to express my gratitude to Prof. Dr. Oskar Paris who made the cooperation with KTH Royal Institute of Technology possible in the first place – without that opportunity this thesis would not exist and my life would look a lot different.

Many thanks also to Dr. Rainer Lechner who supported me during the Covid-19 pandemic lockdown, working in the lab for me when I could not, enabling me to continue my work unhindered and making it possible to finish this thesis now. Likewise, I also want to thank institute technician Peter Moharitsch for the construction of the sample holder used in this thesis making these experiments even possible and my dear friend Sebastian Stock for helping me out as well. Generally, I would like to thank all colleagues at the Institute of Physics that welcomed me so warmly from the first day on and gave me the chance to work in this interesting field of research that is small angle x-ray scattering. That being said I would also like to thank my friends and colleagues at the KTH Royal Institute of Technology for their hospitality and their support during my stay in Stockholm, in particular Prof. Lars Berglund for introducing me to the world of biocomposites and Michel Goy for his invaluable mentoring during my stay in Stockholm.

In closing I would like to thank my friends here in Leoben as well that have made the occasional night-time studying a lot more fun and interesting and that had to remind me from time to time that life is not just about university. Thank you all for being part of the great learning group that we have been!

Eidesstattliche Erklärung

Ich erkläre hiermit, dass ich die vorliegende Arbeit selbstständig verfasst, andere als die angegebenen Quellen und Hilfsmittel nicht benutzt und mich auch sonst keiner unerlaubten Hilfe bedient habe.

Ich erkläre, dass ich die Richtlinien des Senats der Montanuniversität Leoben zu "Gute wissenschaftliche Praxis" gelesen, verstanden und befolgt habe.

Des Weiteren erkläre ich, dass die elektronische und gedruckte Version der eingereichten wissenschaftlichen Abschlussarbeit formal und inhaltlich identisch sind.

Affidavit

I declare in lieu of oath, that I wrote this thesis and performed the associated research myself, using literature cited in this volume.

30.09.2020

Datum

Unterschrift

Abstract

Hierarchically structured materials, found in nature in various forms, often exhibit a complex profile of properties even though they only consist of a rather small spectrum of chemical elements. The variations in their macroscopic properties can be attributed to the structure of the materials and therefore various measuring techniques are required for the characterization of the structure on all levels to be able to exploit the materials' full potential.

In this work composites made from cellulose nanocrystals (CNC) and polyethylene glycol (PEG) were synthesized and characterized using UV-vis spectroscopy as well as small-angle x-ray scattering. The main task of this work was the characterization of the photonic structure of the CNC/PEG composites depending on the polyethylene glycol content in order to gain a better understanding of the optical properties of these films. For this purpose, CNC/PEG composite films with different PEG contents ranging from 0 to 40 weight percent were synthesized and characterized with small-angle x-ray scattering at several angles. It was shown that with increasing amount of PEG the layer spacing of the cholesteric structure increased resulting in a shift of the reflected colour of the films towards red. Further, small-angle x-ray scattering experiments were performed at elevated relative humidity levels to get a deeper insight into the reversible change of the chiral nematic structure of the CNC/PEG composite films on the nanoscale when subjected to humidity.

The subsequent evaluation of the SAXS data in the form of a two-dimensional indirect Fourier transformation (IFT) yielded one-dimensional as well as two-dimensional real space functions out of which structural parameters of the CNC/PEG composite films could be qualitatively extracted.

Kurzfassung

Hierarchisch strukturierte Materialien, wie sie in der Natur in vielfältigster Form vorkommen, weisen oft komplexe Eigenschaftsprofile auf obwohl sie sich nur aus einem geringen Spektrum an chemischen Elementen zusammensetzen. Die Unterschiede in den makroskopischen Eigenschaften sind auf den strukturellen Aufbau zurückzuführen und um das Potential dieser Materialien voll ausschöpfen zu können bedarf es oft mehrerer Messmethoden zur Charakterisierung der Struktur auf allen Ebenen.

In der vorliegenden Arbeit wurden auf Nanozellulose (CNC) und Polyethylenglykol (PEG) basierende Verbundwerkstoffe synthetisiert und anschließend mit UV/VIS-Spektroskopie sowie Röntgen-Kleinwinkelstreuung charakterisiert. Die zentrale Aufgabe dieser Arbeit lag darin den Aufbau der photonischen Struktur der Verbundwerkstoffe in Abhängigkeit vom Polyethylenglykol-Gehalt zu analysieren, um die optischen Eigenschaften dieser Filme besser zu verstehen. Dazu wurden Nanozellulose-Polyethylengykol-Filme mit PEG-Gehalten von 0 bis 40 Gewichtsprozent hergestellt und die Filme unter verschiedenen Winkeln mit Röntgen-Kleinwinkelstreuung untersucht. Es konnte gezeigt werden, dass mit zunehmendem Polyethylenglykol-Gehalt der Abstand zwischen den einzelnen Lagen der cholesterischen Struktur zunahm was zu einer Verschiebung der reflektierten Farbe der Filme in Richtung Rot führte. Um einen besseren Einblick in die reversible Änderung der chiral-nematischen Struktur der CNC/PEG-Filme im Nanometerbereich in feuchter Atmosphäre zu erhalten wurden ebenso Streuexperimente bei erhöhter Luftfeuchtigkeit durchgeführt.

Die anschließende Auswertung der SAXS-Daten in Form einer zweidimensionalen indirekten Fourier-Transformation (IFT) lieferte eindimensionale als auch zweidimensionale Realraumfunktionen aus denen strukturelle Parameter der CNC/PEG-Filme qualitativ erarbeitet werden konnten.

Table of Contents

List of figures

List of abbreviations

Å	Ångström
a.u.	Arbitrary unit
approx.	Approximately
B-spline	Basis spline
CNC	Cellulose nanocrystals
e.g.	Exempli gratia
etc.	Et cetera
i.a.	Inter alia
IFT	Indirect Fourier transformation
kDa	Kilodaltons
MCC	Microcrystalline cellulose
min	Minutes
OLED	Organic light emitting diode
PDDF	Pair distance distribution function
PEG	Polyethylene glycol
rpm	Revolutions per minute
SAS	Small angle scattering
SAXS	Small angle x-ray scattering
SDD	Sample-to-detector distance
UV-vis	Ultraviolet-visible
wt%	Weight percent

1. Introduction

1.1   Relevance of hierarchically structured materials

Hierarchical structures can be found in numerous forms throughout nature with bone, wood and nacre just being a few examples. These hierarchically structured materials exhibit a wide range of unique properties which are mainly related to their structure. [1] The key to successfully synthesize a material with the desired properties therefore lies amongst other things in the control and modification of a materials structure. [2]
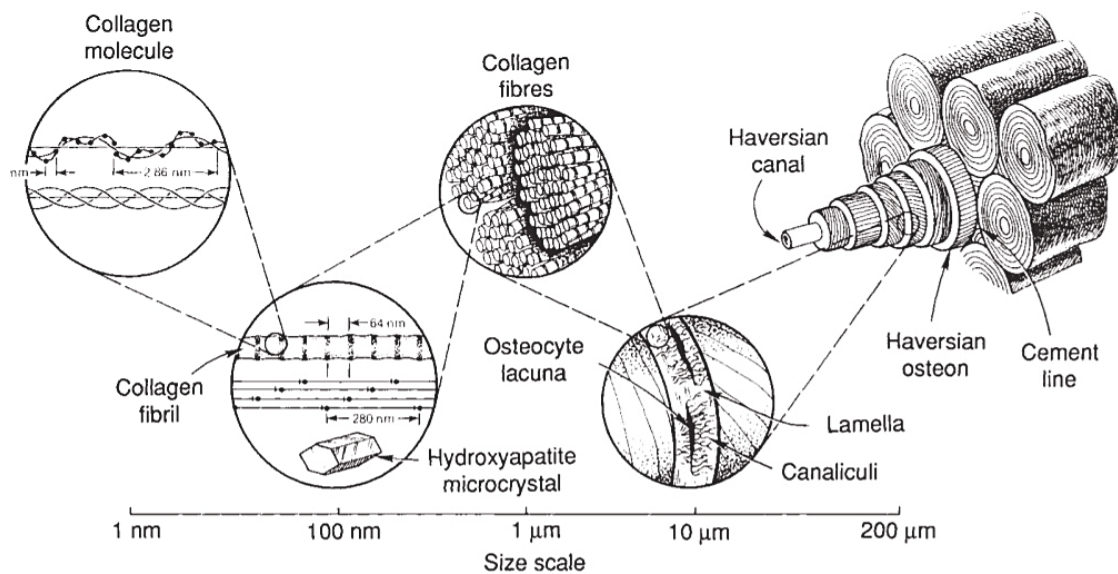
Figure 1: The hierarchical structural levels of bone [2]

The principle of such a hierarchical material can be illustrated for example by human compact bone shown in **Figure 1** having several hierarchical levels from the nanometre to the micrometre-range and eventually on to macroscopic dimensions which lead to its multifunctional profile. At the nanoscale small fibres consisting of collagen and hydroxyapatite are responsible for bones stiffness while the interactions between those two components give bone part of its toughness with cement lines acting as weak interfaces. At larger scales the porous structure plays a vital role in hosting osteocytes, living cells that remodel the bone according to the predominant stresses, while smaller pores containing blood vessels ensure the delivery of nutrients to the tissue. [2] [3]

No other iconic landmark than the Eiffel Tower in Paris has been inspired by the hierarchical structure of bone as Gustav Eiffel was influenced by the work of anatomy professor Hermann von Meyer who had studied how the structure of the thigh bone (femur) enables it to efficiently carry loads. (see **Figure 2**) The mathematical translation of these findings by Karl Cullman then lead to the design of the Eiffel Tower as we know it today.

Owing to its distinctive structure the 324-meter-tall Eiffel Tower only has a relative density of $1.2 \cdot 10^{-3}$ that of iron making it rather lightweight in comparison. [2] [3] [4]
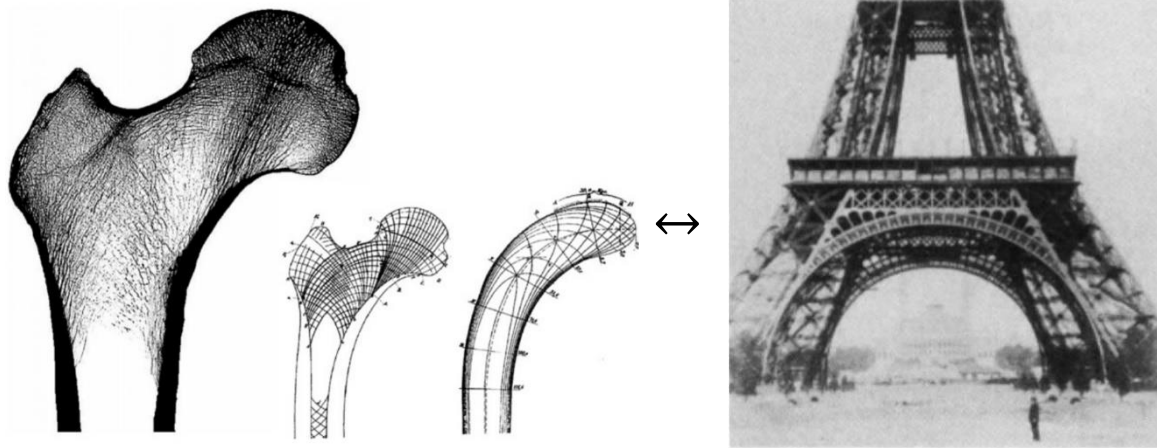
Figure 2: The hierarchical structures of the femur and the Eiffel Tower [2] [3]

The synthesis of multifunctional materials has been ever since of scientific interest and so nanoscopic biological building blocks have also been used to create hierarchical structures. The potential of cellulose based building blocks for hierarchically structured materials was already recognised in the second half of the 20th century as the concentration-dependent hierarchical self-assembly of cellulose microfibrils in aqueous suspensions was detected though understanding of these structures remained limited. [5]

With recent advances in this field several nanocellulose-based composites have been synthesized and functionalized yielding composites with remarkable properties and applications ranging from transparent or conductive paper and flame-retardant devices to incorporation in organic light emitting diodes (OLEDs) or colorimetric sensors. [6] [7] Cellulose nanocrystals seem to be one of the most promising sustainable materials in this context due to their natural abundance and low cost. Furthermore, their ability to self-assemble into photonic structures and their inherent biocompatibility and -degradability makes them ideal for bio-based photonic applications. [7] [8] [9]

1.2   Scope of this thesis

In this work composite films based on cellulose nanocrystals and polyethylene glycol were synthesized and characterized using UV-vis spectroscopy as well as small angle scattering (SAS) or to be more precise small-angle x-ray scattering (SAXS). In order to obtain a better understanding of the change in photonic structure of these films depending on the polyethylene glycol content, films with different PEG contents were characterized with small-angle x-ray scattering at several angles. To get a deeper insight into the reversible change of the chiral nematic structure of the CNC/PEG composites, scattering experiments at elevated relative humidity levels were also performed.

2. Fundamentals

2.1   Interaction of matter with light

At the heart of any scattering technique lies the interaction of an incoming particle like an electron, photon or neutron with the matter to be analysed. As schematically shown in **Figure 3** for a photon of an x-ray beam the interaction can range from absorption, reflection and transmission to the elastic and inelastic scattering of the photon. The type of interaction is dependent on numerous factors including but not limited to the type of material and its thickness as well as beam characteristics. [10] [11] [12]
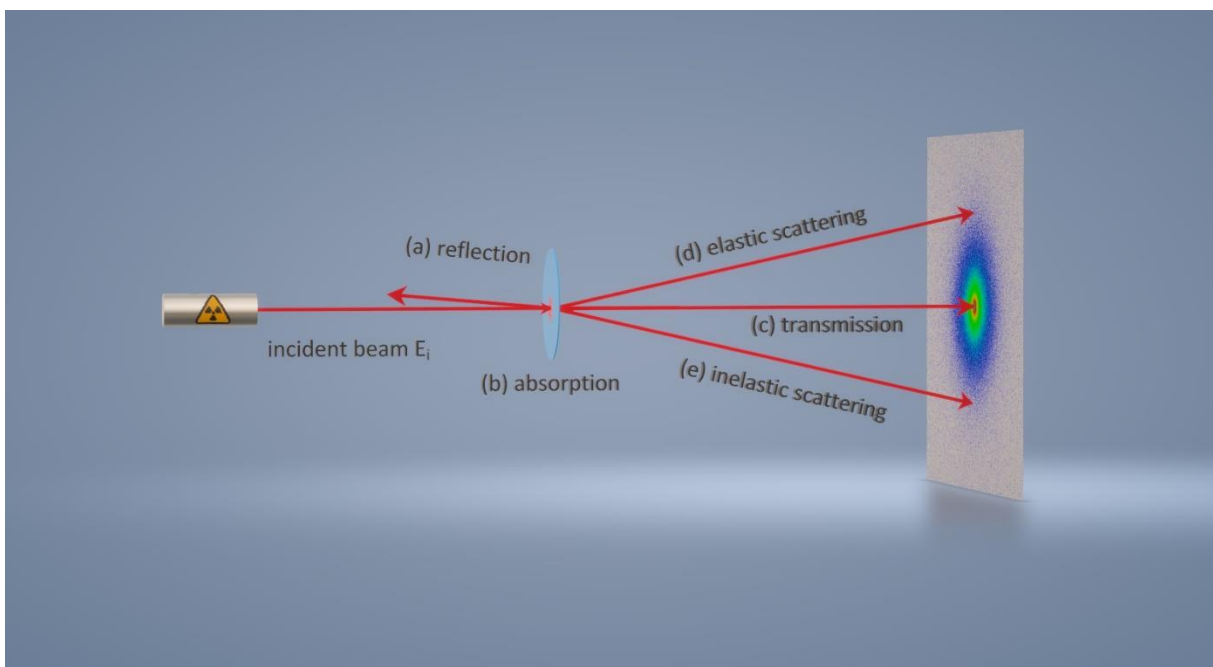
Figure 3: Schematic representation of the different interactions of matter with light: **(a)** reflection **(b)** absorption **(c)** transmission **(d)** elastic scattering ($E_s = E_i$) **(e)** inelastic scattering ($E_s \neq E_i$). Figure adapted and redrawn from [16].

Ultimately all emitted radiation from the analysed material holds some information on the chemical composition or the internal structure of the material but as small angle x-ray scattering experiments were carried out only the theory of elastic scattering of x-rays will be described in the following.

2.2   Scattering theory

2.2.1   Basics

According to the particle-wave dualism x-rays can either be seen as particles (photons) or as electromagnetic waves with wavelengths in the Ångström range and thus x-ray scattering techniques can inherently resolve structures down to the atomic level. Those electromagnetic waves consist of an alternating electric **E** and magnetic field **H** which are perpendicular to the direction of propagation. Omitting the magnetic field for the sake of simplicity leads to the following mathematical description of the electric field in its complex form. [10, 12, 13, 16]

$$\boldsymbol{A}(\boldsymbol{r},t) = A_i \cdot e^{i(\boldsymbol{k}\cdot\boldsymbol{r}-\omega t)} \qquad (1)$$

A_i = initial amplitude of the electric field **E** [V/m]

$\boldsymbol{k}$ = wavevector ($k=2\pi/\lambda$) [m^{-1}]

ω = angular frequency [s^{-1}]

As already illustrated in **Figure 3** the photon can now mainly interact with matter in one of two ways, it can either be absorbed, which is the case for lower x-ray energies, or it can be scattered. Scattering can take place with or without preservation of energy while the propagation direction is altered containing information about the structure of the material. In the case of an elastic scattering event the electromagnetic wave changes its direction of propagation while conserving its energy, which is defined in the following. [10] [12] [16]

$$E = h\nu = \hbar\omega \qquad (2)$$

h = Planck constant [Js]

$\hbar$ = reduced Planck constant [Js]

ν = frequency [s^{-1}]

This change in the direction of propagation can be expressed by the aforementioned wavevector **k** which changes as well in the direction of propagation usually denoted by the scattering angle 2θ. This can be seen in **Figure 4a** and leads to the definition of the scattering vector **q**. [10, 12, 14, 16]

$$\boldsymbol{q} = \boldsymbol{k}_s - \boldsymbol{k}_i \qquad (3)$$

$\boldsymbol{k}_i$ = wavevector of the initial wave [m^{-1}]

$\boldsymbol{k}_s$ = wavevector of the scattered wave [m^{-1}]

Compared to an elastic scattering event the absolute values of the wavevectors differ from each other in the case of inelastic scattering ($|\boldsymbol{k}_i| \neq |\boldsymbol{k}_s|$) while they are otherwise unaffected ($|\boldsymbol{k}_i| = |\boldsymbol{k}_s|$). [12] [14] [16]

For simplicity, the kinematical approximation is assumed in the following, which states that the x-ray is only scattered once assuming that the impinging x-rays are only weakly interacting with the crystal leaving no possibility for the wave to be scattered again before leaving the sample. This assumption is also known as the Born approximation. [12]

a)   b)
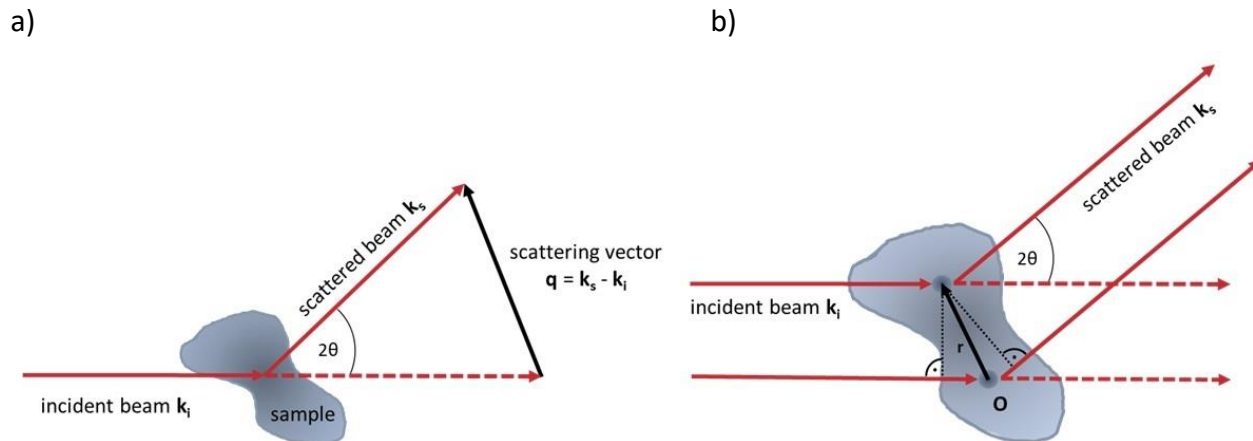
Figure 4: (a) Schematic depiction of the scattering event of an incoming beam k_i which is scattered by an angle 2θ and the scattered beam k_s including the momentum transfer which is also known as the scattering vector q. **(b)** Interference of two waves originating from the origin O and a position $O + r$ depending on the phase difference between the two scattering centres. Figures adapted and redrawn from [12] and [16].

Using a purely classical model, the electron density can be expressed by a number density $ρ(r)$ with the vector r referring to the position of an individual charge (scattering centre). (see **Figure 4b**) The whole scattering can then simply be described by the superposition of all the waves scattered at different volume elements of this electron distribution $ρ(r)$. As already mentioned though, this depends on the phase difference of the scattered waves, which in the case of **Figure 4b** for the scattering centres at positions O and $O + r$ can be expressed by equation 4. [12] [15] Whether the scattered waves interfere constructively (in phase) or destructively (out of phase) is not only dependent on the scattering angle 2θ then but also on the orientation as well as the distance of the scattering centres as seen from equation 4. [10]

$$\Delta\varphi(r) = (k_i - k_s) \cdot r = q \cdot r \qquad (4)$$

If the wavelength λ is known, the scattering vector q can be described by the scattering angle 2θ as depicted in the triangle in **Figure 4b** leading to the following expression for its magnitude. [12] [14]

$$|q| = 2|k|\sin\theta = \frac{4\pi}{\lambda} \cdot \sin\theta \qquad (5)$$

This is commonly done in small-angle x-ray scattering experiments as scattering patterns (intensity I) are commonly plotted as a function of the scattering vector q thus eliminating the wavelength. [10] [14]

The amplitude of the scattered wave can be expressed by the Fourier transform of the electron density distribution

$$A(\boldsymbol{q}) = \int_0^V \rho(\boldsymbol{r}) \cdot e^{(-i \cdot \boldsymbol{q} \cdot \boldsymbol{r})} dr \qquad (6)$$

and vice versa the electron density can be obtained from the inverse Fourier transform of the scattering amplitude. [14] [15]

$$\rho(\boldsymbol{r}) = \frac{1}{(2\pi)^3} \int A(\boldsymbol{q}) \cdot e^{(i \cdot \boldsymbol{q} \cdot \boldsymbol{r})} dq \qquad (7)$$

The intensity *I(q)* can then be calculated by squaring the amplitude *A(q)* of the scattered wave leading to the following definition in reciprocal space (also called q space). [14] [15]

$$I(\boldsymbol{q}) = A(\boldsymbol{q}) \cdot A(\boldsymbol{q})^* = \int \int \rho(\boldsymbol{r_1}) \cdot \rho(\boldsymbol{r_2}) \cdot e^{-iq(r_1 - r_2)} dr_1 dr_2 \qquad (8)$$

I(q) = intensity [a.u.]

A(q) = amplitude of the scattered wave [V/m]

A(q)* = complex conjugate of *A(q)* [V/m]

Integrating equation 8 in a two-step process, starting with the summary of all the pairs of scattering centres with equal relative distance and then integrating over all possible relative distances comprising the phase factor clearly illustrates the reciprocal relationship between ordinary and reciprocal space. The integration over all the possible relative distances consequently yields the intensity distribution in reciprocal space which is a Fourier transform.

$$I(\boldsymbol{q}) = \int \tilde{\rho}^2(\boldsymbol{r}) \cdot e^{-i \cdot \boldsymbol{q} \cdot \boldsymbol{r}} dr \qquad (9)$$

$\tilde{\rho}^2(\boldsymbol{r})$ = density of all electron pairs with the same relative distance *r* [e⁻/m³]

The electron density of all the electron pairs with the same relative distance $\tilde{\rho}^2(\boldsymbol{r})$ can then be expressed vice versa by the inverse Fourier transform of *I(q)*.

$$\tilde{\rho}^2(\boldsymbol{r}) = \left(\frac{1}{2\pi}\right)^3 \int I(\boldsymbol{q}) \cdot e^{i \cdot \boldsymbol{q} \cdot \boldsymbol{r}} dq \qquad (10)$$

Assuming a statistically isotropic system further simplifies equation 9 by taking the spherical average over all directions of *r* for the phase factor.

$$\langle e^{-i \cdot \boldsymbol{q} \cdot \boldsymbol{r}} \rangle = \frac{\sin(q \cdot r)}{q \cdot r} \qquad (11)$$

This orientational average, first derived by Debye in 1915 [17], is represented here by angle brackets $\langle \dots \rangle$ and yields in combination with equation 9. [12] [15]

$$I(q) = \int 4\pi r^2 \cdot \tilde{\rho}^2(r) \cdot \frac{\sin q \cdot r}{q \cdot r} dr \qquad (12)$$

As implied by the previous equations reciprocal and real space are simply connected by the phase $q \cdot r$ meaning that the result is the same whether r is large and q is small or the other way round. This is of great importance as it shows that small particles (smaller r) will give rise to diffraction patterns across the q-range (greater q) and larger particles (bigger r) on the other hand will lead to diffraction patterns situated at smaller angles (lesser q). [15]

It has to be noted, that it is not the electron density that makes a contribution to the detected diffraction pattern in the end but rather the fluctuations around the mean electron density that lead to a signal. [10] [15]

2.2.2   Small angle x-ray scattering

Small angle x-ray scattering refers to an analytical non-destructive technique for the determination of structural features of a sample by elastic scattering of x-rays. X-rays are recorded at small angles, typically around 0.1° to 10°, giving SAXS its name. As already emphasized before larger particles or structural features give rise to scattering at smaller angles and so according to the reciprocity law typically structures between ~0.5 nm and ~100 nm can be resolved in the angular range of SAXS depending on the experimental setup. As the beam itself illuminates more than one particle in the sample volume though the scattering patterns contain information about the average particle sizes or shapes in the sample. The resolution of these average structural parameters depends on several factors including but not limited to the pixel size of the detector, the sample-to-detector distance (SDD) as well as the size of the beam stop and the photon energy. **Figure 5** shows such a schematic small angle x-ray scattering setup featuring a few of the aforementioned resolution limiting factors. [10] [14] [15]
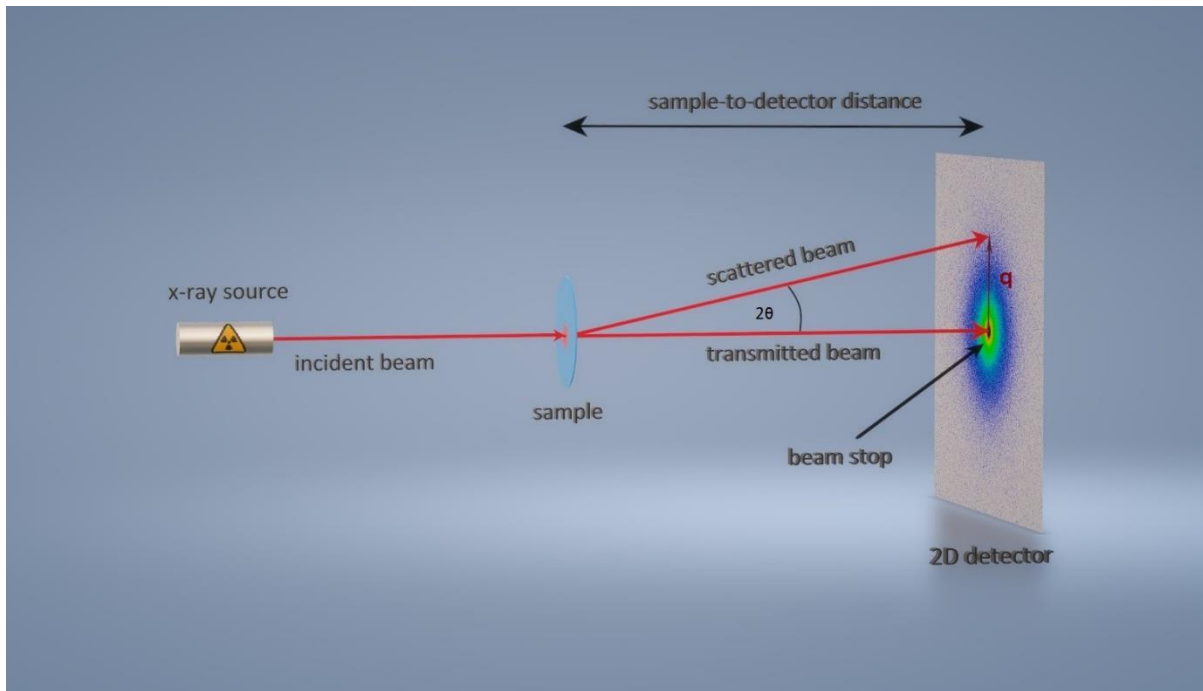
Figure 5: Schematic representation of a small angle x-ray scattering setup. Figure adapted and redrawn from [16].

The total scattered intensity detected from a system of identical particles can be calculated as shown in the following [10] [16] [18]

$$I(\boldsymbol{q}) = N \cdot V^2 \cdot \Delta\rho^2 \cdot P(\boldsymbol{q}) \cdot S(\boldsymbol{q}) \qquad (13)$$

N	= number of particles [-]
V	= volume of a particle [m^3]
Δρ	= fluctuations of the scattering length density [m^{-2}]
P(q)	= form factor [-]
S(q)	= structure factor [-]

including two important factors, namely the form factor *P(q)* and the structure factor *S(q)*, containing information about the inner structure of the sample. The form factor *P(q)* obviously comprises information about the morphology - size, shape and internal density distribution - of the particles while the structure factor *S(q)* holds information about inter-particle interactions like the degree of order as well as the distances between particles. In a dilute system particle-particle interactions can be neglected and equation 13 is simplified as the structure factor *S(q)* ≈ 1. It has to be kept in mind though that the information gained about the structure is only accurate for particles having a narrow size distribution as with increasing polydispersity an average scattering pattern is obtained due to the summary of the different form factors of all the particle sizes. [10] [12] This can lead to ambiguities, since for example

the scattering pattern of a non-spherical object can be identical to the one of polydisperse spheres. [20]

An important thing to keep in mind as well is that in scattering experiments only the intensity can be measured while the amplitude cannot be obtained which leads to a loss of the phase of the electric field. Hence, knowledge about the structure from e.g. complementary experimental techniques is required beforehand for the unambiguous interpretation of the data. [10]

2.3   SAXS analysis

A proper analysis of a small angle x-ray scattering experiment starts with processing of the detected scattering data. As already mentioned before the intensity *I* is usually depicted as a function of the scattering vector *q* leading to a two-dimensional scattering pattern as shown in **Figure 5**. Before this data can be interpreted though any additional scattering not originating from the sample needs to be corrected. Basically, anything in the pathway of an x-ray beam leads to scattering and thus a background correction is necessary. To keep undesirable scattering to a minimum and reduce the influence of the primary beam tails the sample-to-detector distance should therefore ideally be in vacuum as even air produces scattering.

Taking a closer look at the mathematical expression of the scattering intensity *I(q)* (equation 13) it is evident that it consists of three parts.

$$\Delta I_{abs}(\boldsymbol{q}) = K \cdot P(\boldsymbol{q}) \cdot S(\boldsymbol{q}) \qquad (14)$$

$\Delta I_{abs}(\boldsymbol{q})$ = background corrected intensity [cm^{-1}]
K = constant [cm^{-1}]

K contains all the constant terms, e.g. the number of the particles and their volume etc., while *P(q)* and *S(q)* represent the angle dependent form and structure factor. The information on the structural parameters of the particles consequently lies in the latter two factors. **Figure 6** shows the dependence of the form factor *P(q)* on the scattering vector *q* indicating what kind of information can be found over the q range with regimes each corresponding to a certain range of scattering vectors or taking equation 5 into account a spectrum of wavelengths. [10] However, only for the utmost simple cases the form factor *P(q)* can be calculated analytically. For a single particle it can be expressed in the following way.

$$P(\boldsymbol{q}) = \frac{1}{V} \int_{V} e^{i \cdot \boldsymbol{q} \cdot \boldsymbol{r}} dV \qquad (15)$$

When analytical methods are not feasible anymore then numerical evaluation of the integrals is needed. [12]
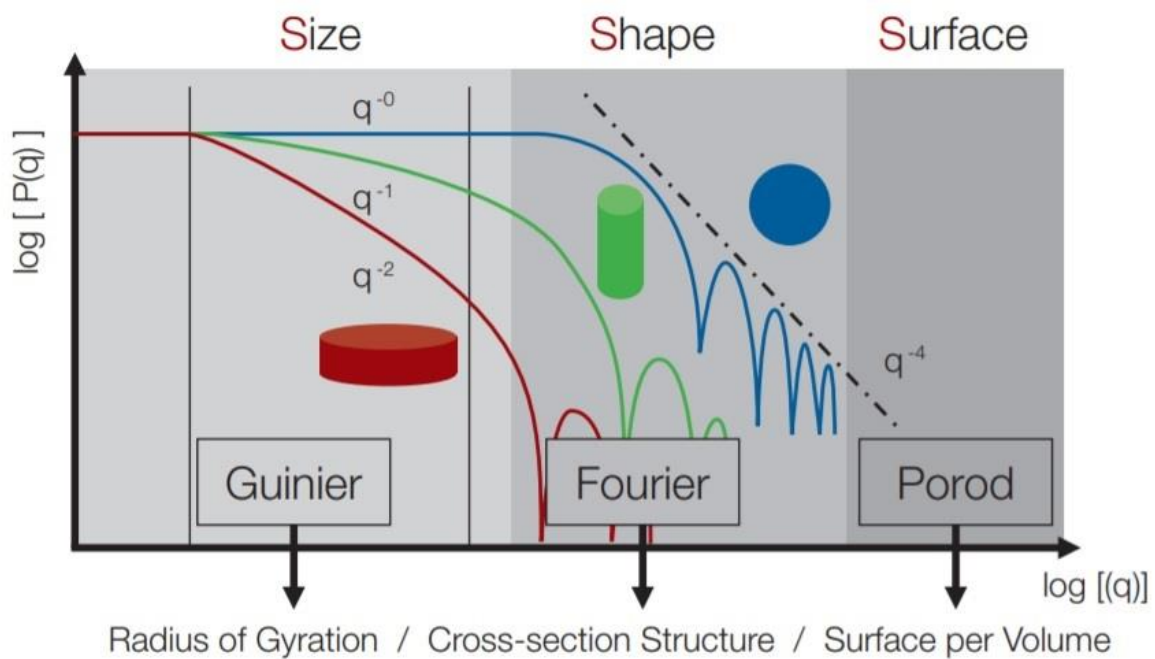
Figure 6: Dependence of the form factor *P(q)* on the scattering vector *q* for three basic particle shapes, namely a disc (red), a cylinder (green) and a sphere (blue). Furthermore, the division of the q range in the Guinier, Fourier and Porod regimes is included showing which information can be obtained from the corresponding domains. Figure adapted from [10]

2.3.1 Guinier Analysis

At smaller q or vice versa in the long-wavelength limit ($qR \rightarrow 0$) the form factor can be described by a Gaussian curve leading to the following expression for the scattering intensity of a single spherical particle.

$$I_P(q) \approx \Delta\rho^2 \cdot V^2 \cdot e^{-\frac{q^2 \cdot R^2}{5}} \qquad (16)$$

R = radius of the particle [m]

As can be clearly seen the radius of the particle can be obtained by plotting the logarithm of the scattering intensity log *I(q)* over the squared scattering vector q^2. The radius can then be extracted from the slope of the linear function which is equal to $-\frac{R^2}{5}$. It has to be kept in mind though that this is only valid for a dilute system of spherical particles. For the analysis of a system with particles of a different shape a more general expression, the so-called radius of

gyration is used. It is defined as the quadratic mean distance from the centre of gravity of a particle and its mathematical expression is given in the following. [10] [12]

$$R_G{}^2 = \frac{\int_V \rho(r_i) \cdot r_i^2 \, dV_i}{\int_V \rho(r_i) \, dV_i} \qquad (17)$$

R_G = radius of gyration [m]

While the integrals typically have to be solved numerically, the radius of gyration of a sphere can be given directly by $R_G^2 = \frac{3}{5}R^2$ and using this expression equation 16 can be rewritten as shown below.

$$I_P(q) \approx \Delta\rho^2 \cdot V^2 \cdot e^{-\frac{q^2 \cdot R_G{}^2}{3}} \qquad (18)$$

As Guinier was the first to come up with the approximation of the form factor *P(q)* by a Gaussian curve leading to the derivation of equation 16 the analysis of this part of the q range was named after him. The corresponding Guinier regime can be seen on the left-hand side of **Figure 6**. [10] [12] [15]

2.3.2   Porod Analysis

At the other end of the q range or vice versa in the short-wavelength limit ($qR \gg 1$) the scattering intensity of a single spherical particle can be expressed by applying Porod's law

$$I(q) = \frac{2\pi\Delta\rho^2}{q^4} \cdot S \qquad (19)$$

S = surface of a sphere [m^2]

and so according to equation 19 the surface area of the particles can be investigated by looking at the scattering intensity at larger *q*. Similar to the lower end of the q range this regime at shorter wavelengths is named Porod regime referring to its analysis method and can be seen on the right-hand side of **Figure 6**. [12] [14]

2.3.3   Transformation techniques

Last but not least the third regime situated between the Guinier and Porod domains provides information about the particles' shape as well as their internal density distribution. This regime named after Fourier makes up the central part of **Figure 6**.

A simple and quick estimation of the particles' shape can be made by looking at the power law of the form factor *P(q)* in the middle part. As depicted in **Figure 6** in a double logarithmic representation the initial slope holds information about the dimension and in consequence shape of a particle with a globular particle (zero-dimensional) displaying a slope of 0, a cylindrical particle (one-dimensional) having one of -1 and a lamellar particle (two-dimensional) possessing a slope of -2. In addition, the slope in this q range also holds information about the resolution limit of the scattering experiment as a steeper slope of e.g. -4 indicates that the particles illuminated are too large to be resolved. [10]

Further information can be extracted from the central part of the scattering intensity *I(q)* by its transformation into real space which in mathematical terms is similar to a Fourier transformation. [10] [19] [21]

$$I(q) = 4\pi \int_0^\infty p(r) \cdot \frac{\sin q \cdot r}{q \cdot r} dr \qquad (20)$$

p(r)   = pair distance distribution function [m^{-3}]

This results in the so-called pair distance distribution function, or short PDDF, which in essence contains the same information as the scattering intensity *I(q)* with the major difference of being in real space. Consequently, structural information like the size and shape of a particle can be obtained directly from the PDDF. [22] As the pair distance distribution function can be interpreted as a histogram of all the inter-particle distances, particles with different shapes can be easily distinguished as shown in **Figure 7**. [10] [21]
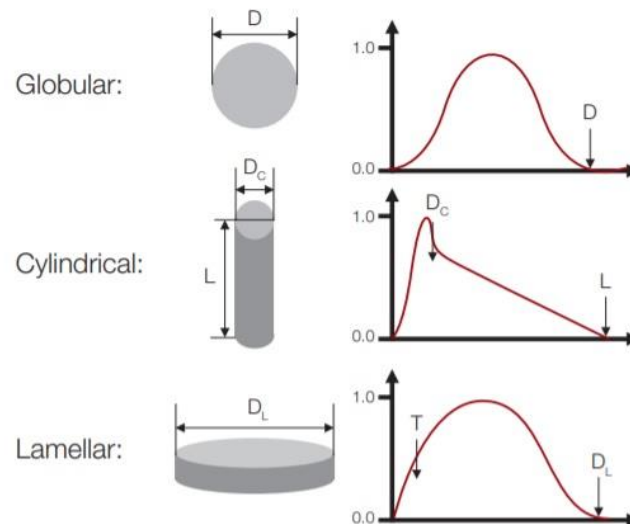
Figure 7: Pair distance distribution functions for a globular, a cylindrical and a lamellar particle indicating which structural parameters can be directly obtained from the PDDFs. Corresponding scattering curves are shown in the preceding figure. [10]

As can be seen in **Figure 7** a bell-shaped peak is characteristic for spherical particles while an overshooting peak followed by a linear tail indicates a cylindrical particle shape. Lamellar particles on the other hand exhibit a different PDDF making a distinction easily possible. One thing that all PDDFs have in common though is their decay to 0 with increasing distance marking the largest dimension of the analysed particle. [10] [22]

a)   b)
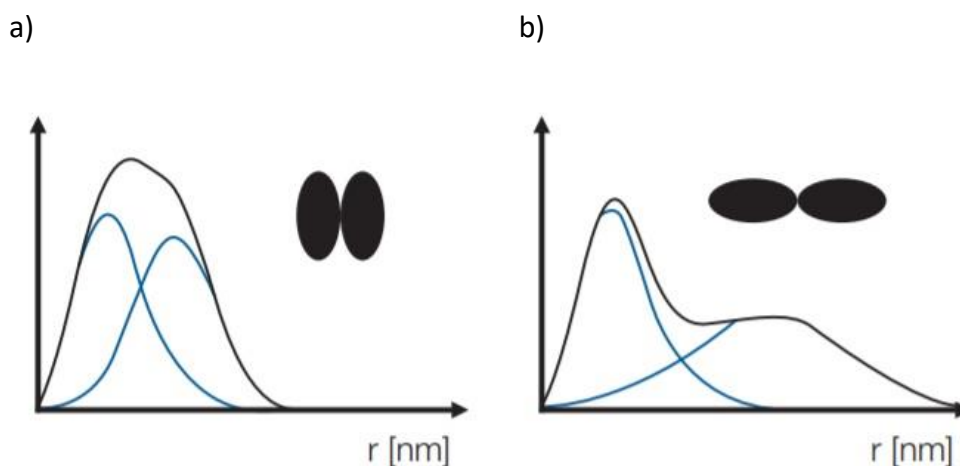
Figure 8: Pair distance distribution functions of dimers consisting of two elliptical monomers in a **(a)** parallel arrangement or in a **(b)** linear arrangement with the black curves depicting the dimers and the blue curves representing the PDDFs of the monomers as well as the difference between the aforementioned PDDFs. [10] [22]

As illustrated in **Figure 8** the analysis of PDDFs also proves useful in the investigation of aggregation as the PDDF of an aggregate can be recognized by the appearance of a second peak. It has to be taken care though as any PDDF can be made up of a distribution of

polydisperse particles of arbitrary shape and so complementary experiments should always be carried out additionally for the unambiguous determination of the structural parameters. [10] [22]

The most common way of obtaining a pair distance distribution function is by applying the indirect Fourier transformation (IFT) technique developed by Glatter [19]. This single step procedure is well suited for the impartial interpretation of the scattering data as it not only requires minimum knowledge in advance but also does not make use of any models. **Figure 9** gives an overview on the indirect Fourier transformation technique.
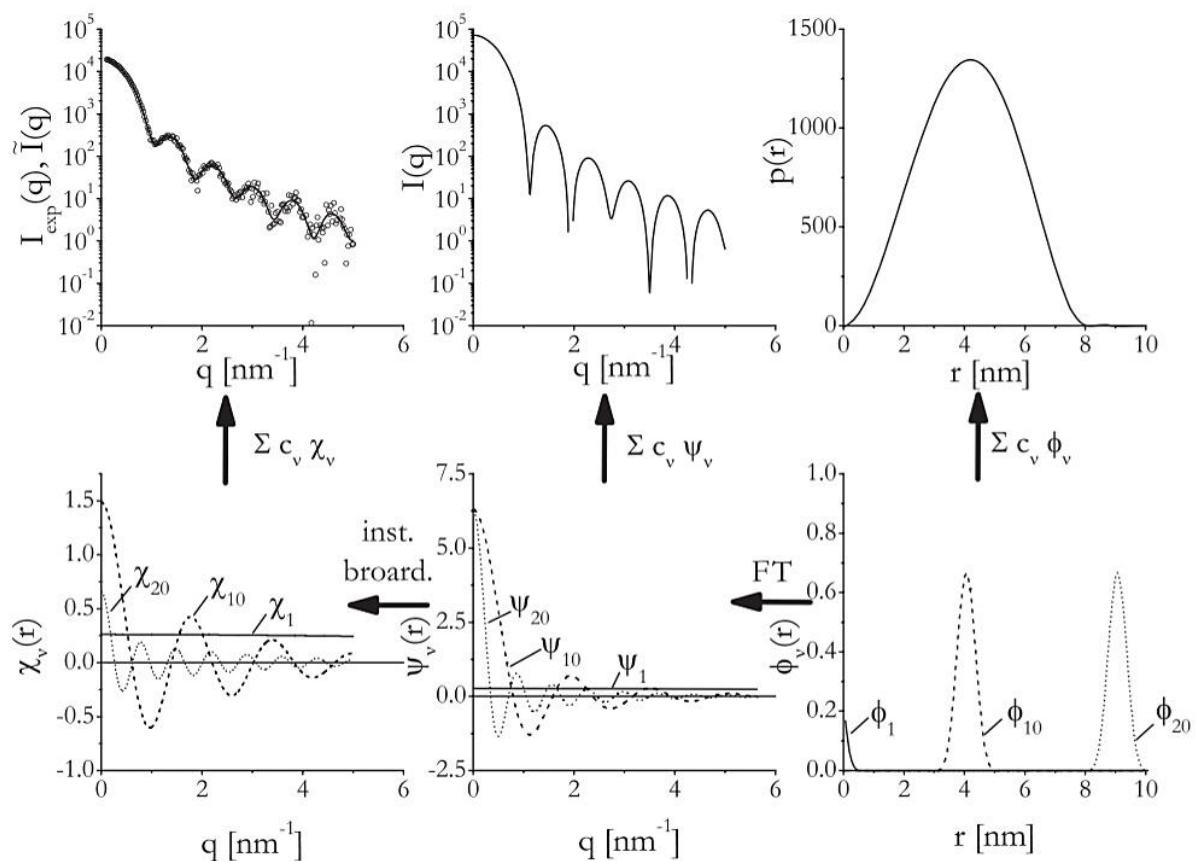
Figure 9: Schematic representation of how the indirect Fourier transformation works: After a set of cubic B-splines has been defined (**bottom right**), they are Fourier transformed (**bottom centre**) and smeared (**bottom left**). A subsequent approximation of these Fourier transformed and smeared splines to the experimental scattering curve yields the coefficients c_v which then can be used to calculate the PDDF (**top right**) owing to the linear nature of all the transformations involved. [21]

The straightforward calculation of the PDDF from the experimental scattering curve by elimination of any instrument related broadening effects and the Fourier transformation is unfortunately not possible due to the limited q range experimentally available as well as the difficult calculation of the desmeared scattering curve. [21]

The elementary principle at the core of the indirect Fourier transformation is the representation of *p(r)* by a sum of *N* cubic B-splines as basis functions up to a limiting dimension D_{max}. In a similar fashion to equation 20 the scattering intensity *I(q)*, now expressed by the sum of the transformed functions $\psi_v(q)$, can be calculated by Fourier transformation of the basis functions $\varphi_v(r)$. [15] [21] [26]

$$\psi_v(q) = 4\pi \int_0^\infty \varphi_v(r) \cdot \frac{\sin q \cdot r}{q \cdot r} dr \qquad (21)$$

Comparing equation 20 and 21 the representation of *p(r)* by the sum of basis functions $\varphi_v(r)$ can be clearly seen. As a perfect instrument is assumed in this case, the Fourier transformed functions $\psi_v(q)$ need to be smeared accounting for any instrument related broadening effects leading to the new functions $\chi_v(q)$. The experimental scattering curve *Iexp(q)* can then be expressed by the sum of the smeared functions $\tilde{I}(q)$ yielding the following. [21]

$$p(r) = \sum_{v=1}^N c_v \cdot \varphi_v(r) \qquad I(q) = \sum_{v=1}^N c_v \cdot \psi_v(q) \qquad I_{exp}(q) \approx \tilde{I}(q) = \sum_{v=1}^N c_v \cdot \chi_v(q)$$

$$(22) \qquad\qquad\qquad (23) \qquad\qquad\qquad (24)$$

Fitting of the sum of the smeared basis functions $\chi_v(q)$ to the experimental scattering data is usually done in a least-squares approximation but as the least-squares problem is itself unstable due to experimental uncertainties and the limited q range experimentally available the equation system needs to be stabilised. This is done in the form of stabilisation matrices with parameters, the so-called Lagrange multipliers, which are measures for the strength of the stabilisation and are varied in order to determine the correct stabilisation parameter. The equivalence of the factors c_v is guaranteed by the linear nature of all the transformations involved and at last after stabilisation these factors c_v can be used to directly obtain the PDDFs as well as the scattering curve *I(q)* free of any instrument related broadening effects. [21] [23] [31]

It should be pointed out that the indirect Fourier transformation as described above can not only be performed in one dimension but also in two dimensions as was first presented by Gerhard Fritz-Popovski using two-dimensional basis functions. These basis functions in real space are usually expressed in circular coordinates by two sets of cubic B-splines, one along the radial *r* scale and the other one along the angular χ scale. The third dimension is neglected at smaller angles, however, as the component of **q** in the beam direction is rather small compared to the other components. Thus, the resulting two-dimensional real space functions

obtained by the 2D IFT are nothing else than the two-dimensional projections of the three-dimensional real space functions. [23]

Another real space function commonly used in the analysis of the scattering curve is the (radial) autocorrelation function $\gamma(r)$ also known as the correlation function or simply $\gamma(r)$. Just as the pair distance distribution function it contains information on the structural parameters of the particles and the two are even related to each other as shown in the following with $X = 2$ in the three-dimensional and $X = 1$ in the two-dimensional case. [15] [19] [23]

$$p(r) = \gamma(r) \cdot r^X \qquad (25)$$

The correlation function can be interpreted as the overlap of the volume of the particle and a copy of the volume of the particle, displaced by the vector **r**, weighted by the scattering length density fluctuations at every point in the two volumes of the particle and its "ghost" as schematically shown in **Figure 10**. To put it more simply, $\gamma(r)$ can be understood as the averaged probability of finding oneself in the same particle again after having started in the particle and then having "jumped" a distance described by the vector **r**. [15] [24]
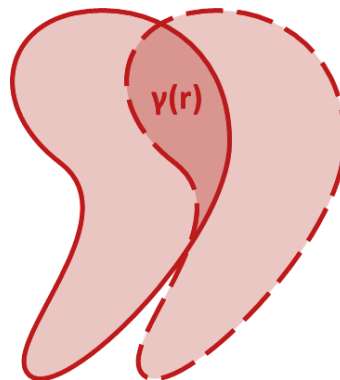
Figure 10: Interpretation of the autocorrelation function represented by the overlap of the particle and its "ghost". Figure adapted and redrawn from [25].

While structural parameters of particles can sometimes be found easily in real space or reciprocal space, at the same time they might not even be visible in the other one. Consequently, for a proper analysis of the scattering data it is necessary to compare the curves from both real and reciprocal space for a more thorough interpretation of the results. [23]

3. Experimental

3.1 Synthesis of the CNC/PEG composites

All CNC/PEG composite samples used in this thesis were synthesized at the KTH Royal Institute of Technology in Stockholm, Sweden in a cooperation with the Montanuniversität Leoben in Austria and the synthesis was based on the processing conditions given in [7], [27] or [28] respectively.

3.1.1 Preparation of the cellulose nanocrystal suspension

Avicel microcrystalline cellulose (MCC) PH-200 provided by FMC BioPolymer was used as a starting material for the synthesis of the cellulose nanocrystals.

For the subsequent sulphuric acid hydrolysis of the microcrystalline cellulose a sulfuric acid solution of 64 wt% was prepared by mixing 95-98% sulphuric acid from VWR with ultrapure water. In this way 270 ml of the sulphuric acid solution were prepared by slowly pouring the sulphuric acid into the ultrapure water while continously mixing the two components. Extreme caution had to be exercised though as the reaction of sulphuric acid and water is highly exothermic [29] and thus the beaker was set into a box of dry ice to ensure optimal cooling during mixing. In the following 30 g of MCC were taken and gradually added to the 270 ml of sulfuric acid solution while stirring corresponding to an acid-to-MCC ratio of ∼ 9 ml per gram. The mixture was then stirred for around 35 minutes at a temperature of 45°C enabling the adjustment of the sulphur content of the cellulose nanocrystals and in further consequence the surface charge density. If done correctly the suspension exhibited an ivory colour and displayed a slight yellow shimmer at the end of mixing.

The hydrolysis was then stopped by diluting it 15-fold with deionized water and afterwards the solution was left to settle for at least 12 hours so precipitation of the nanocellulose could occur. In order to concentrate the CNC and remove any aqueous acid left the suspension was centrifuged at 4300 rpm for 10 min at room temperature. After the centrifugation the remaining solution was poured away and only cellulose nanocrystal precipitates remained which were stirred for ∼30 min to ensure homogeneity.

Next the precipitated cellulose nanocrystals were dialyzed against deionized water for seven days to remove any solutes having a small molecular weight from the CNC precipitate. For that the CNC was filled in dialysis tubes that were clamped shut at each end and submerged in a bucket filled with deionized water. Only a third of the bags was filled with the CNC precipitate

allowing a little deionized water to flow through the dialysis tubes over time. In order to disperse the CNCs after the dialysis the suspension was sonicated at 60% output until it turned transparent. For the sonification of ~ 300 ml each a Branson Sonifier Model 250 ultrasonic cell disruptor/homogenizer or a Sonics Vibra-Cell VCX 750 ultrasonic processor was used with a tip diameter of 12 or 13 mm respectively while the suspension was cooled by a surrounding water bath. Finally the aqueous CNC suspension was concentrated to 3 wt% by letting it evaporate at room temperature.

3.1.2 Preparation of the polyethylene glycol suspension

As a starting material PEG with a molecular mass of ~ 20 kDa produced by Merck was used. For the synthesis of 150 ml of a 10 wt% PEG suspension 15 g of polyethylene glycol were taken and gradually added to 135 ml of ultrapure water while the suspension was continously stirred at 60°C. After PEG had been gradually added and it had dissolved, the solution was further mixed for at least 12 hours to ensure homogenity.

3.1.3 CNC suspension + PEG suspension → CNC/PEG composite films

The desired amounts of the prepared aqueous CNC (3 wt%) and PEG (10%) solutions were measured and mixed together for several minutes. In this way composites with varying weight ratios of CNC and PEG ranging from 100/0 to 60/40 were prepared using different amounts of CNC and PEG solution. The mixed solution was subsequently sonicated for 30 seconds at 40% output and stirred for another 24 hours to ensure a homogenous mixture.

Finally the CNC/PEG suspension was cast into a petri dish with a diameter of 9 cm and was then dried at room temperature until all water had evaporated which could take up to several days yielding a colourful film as exemplary shown in **Figure 11**. While drying close attention had to be paid to the surrounding environment as already a small air flow could cause a disturbance in the self-assembly of the cellulose nanocrystals. Ideally the drying CNC/PEG suspensions were therefore put into a closed ventilated cabinet for the entire duration to minimize the effect of any disturbances. To guarantuee uniform drying of the CNC/PEG suspensions the petri dishes were elevated to ensure air flow underneath as well. As a reference value a total dry mass of ~ 400 mg was taken for a CNC/PEG composite film with a diameter of 9 cm.
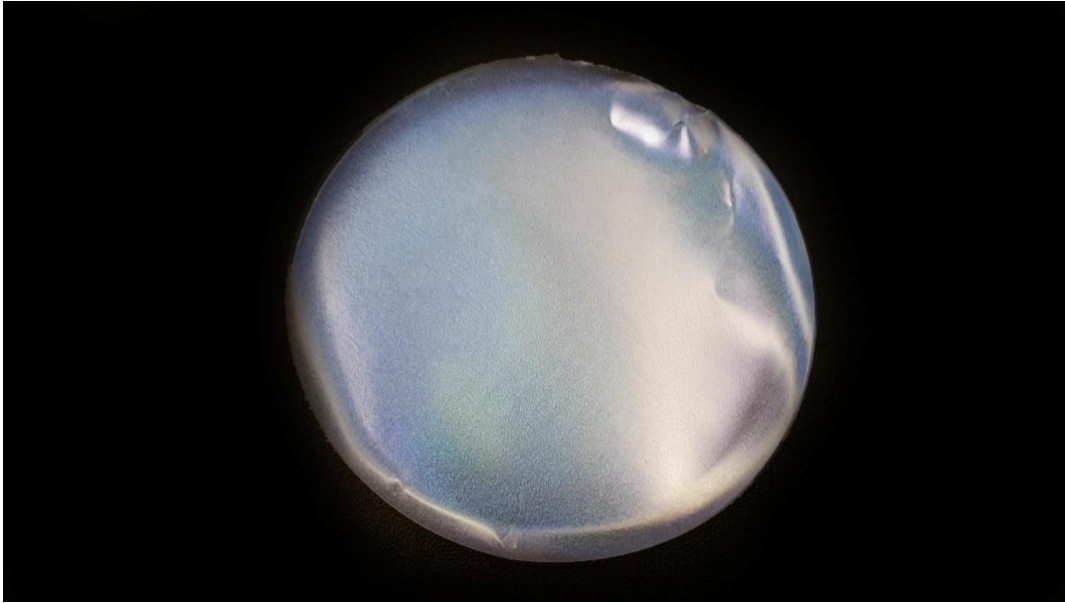
Figure 11: Photograph of a CNC/PEG (90/10) composite film illuminated by white light

3.2 Characterisation of the CNC/PEG composites

3.2.1 UV-vis spectroscopy

To characterize the shift in reflectance of the CNC/PEG composite films with the addition of polyethylene glycol UV-vis spectroscopy was carried out at the KTH Royal Institute of Technology in Stockholm using a Varian Cary 50 Bio UV–visible spectrophotometer. The films were mounted perpendicular to the beam and transmission spectra were collected in dual beam mode in the wavelength range of 200 – 800 nm.

3.2.2 Small angle x-ray scattering

All small angle x-ray scattering experiments were carried out at the Montanuniversität Leoben in Austria on a NANO-STAR laboratory instrument by Bruker AXS with an Incoatec IµS microsource using Cu-Kα radiation with a wavelength of ~ 1.5418 Å. The beam was collimated by 300 µm SCATEX pinholes and the obtained scattering patterns were detected using a VÅNTEC-2000 detector (2048 x 2048 pixels) by Bruker AXS at sample-to-detector distances of 675 mm and 1052 mm. For the calibration of the sample-to-detector distances silver behenate was used due its set of well-defined and evenly distributed diffraction peaks at low angles. [30] The SAXS experiments of the CNC/PEG composite films were performed in transmission geometry while the sample holder was mounted on a precision rotation stage PI M-116 enabling measurements at various angles to the direction of the primary beam. As shown in **Figure 12** a sample holder was specifically constructed for this so that the films could be measured free-standing.
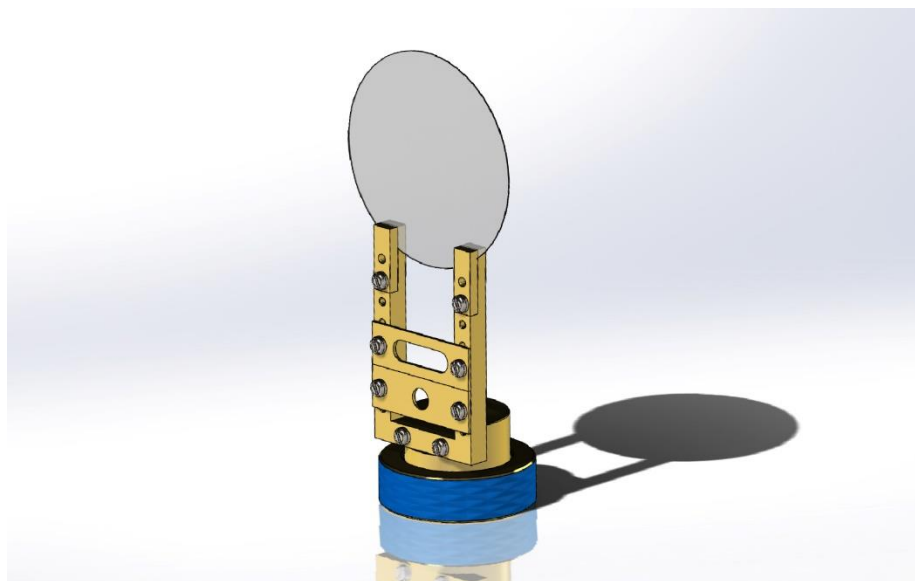
Figure 12: Sample holder constructed for CNC/PEG composite films with a diameter of ∼9 cm

After evacuation of the sample chamber a 2D nanography was always performed first to locate a suitable position for the measurement and to ensure that the location chosen was representative for the sample, e.g. that no structural inhomogeneities were sampled. Transmission experiments were then carried out at 2 to 6 different positions on each specimen at different angles to the sample varying from 0° to 85° whereas 0° referred to the sample being perpendicular to the beam direction and 90° corresponded to the film standing parallel to the beam direction. To ensure that the same position was measured at each angle a positional correction was implemented and in the same way the exposure time was also corrected as at higher angles the beam travelled a longer distance through the sample. Measurement times therefore ranged between 0.5 hours and 1.5 hours.

Moreover, transmission experiments were also carried out at elevated relative humidity levels under ambient pressure. This was achieved by putting an open container filled with water into the sample chamber and performing the measurement after equilibrium had been reached. These transmission experiments were performed at the longer SDD of 1052 mm as compared to the scattering experiments of the dry samples described above which were carried out at a sample-to-detector distance of 675 mm.

In addition to the scattering of the samples at each measuring point the scattering of the samples plus glassy carbon and of glassy carbon without the samples were determined as well for the subsequent correction of absorption effects of the scattering data.

3.3   SAXS data evaluation

In this thesis several software, e. g. *MULIP SAXS 2D*, *PCG Tools*, *PCG GIFT, PCG IFT2D* and *PCG Viewer 2D* which were all developed by my supervisor Gerhard Fritz-Popovski, were used for the processing of the SAXS data.

3.3.1   MULIP SAXS 2D

The 2D SAXS data of the CNC/PEG composite films was first corrected in *MULIP SAXS 2D* starting with an adjustment of the beam centre and calibration of the sample-to-detector distance with the help of silver behenate. Afterwards any transmission effects of the CNC/PEG composite films were accounted for by using the scattering of glassy carbon which is often used as an intensity calibration standard in small angle scattering due to its long-term stability during use and significant scattering. [32] The transmission of the CNC/PEG composite films could then be determined by division of the integrated intensities of the film and glassy carbon and the one of glassy carbon itself. [11] At last the background scattering pattern which had been detected without the sample was subtracted completing the correction of the acquired scattering patterns of the CNC/PEG composite films.

After the scattering data had been corrected one dimensional scattering curves *I(q)* were obtained by cake integration. In this way 180 radial integrations were computed for each measuring point from 0° to 180° over most of the q range available from approx. 0.1 nm^{-1} to 3.17 nm^{-1} for the dry samples and from approx. 0.04 nm^{-1} to 2.04 nm^{-1} for the samples at increased relative humidity in accordance with the chosen SDDs. It has to be noted in this context that due to the centrosymmetry of the scattering patterns it was sufficient to only perform cake integrations from 0° to 180° corresponding to a semicircle. Only the scattering patterns measured at 0° to the primary beam were radially integrated from 0° to 360° yielding one dimensional scattering curves *I(q)* which were further processed in *PCG Tools* and *PCG GIFT*.

3.3.2   PCG Tools

The one dimensional scattering curves *I(q)* measured at 0° to the primary beam were then normalized to the same area and afterwards the scattering curves from each measuring point were averaged in *PCG Tools*.

3.3.3 PCG GIFT

The averaged one dimensional scattering curves *I(q)* computed in *PCG Tools* were then further processed in *PCG GIFT* where they were used for the indirect Fourier transformation yielding one dimensional pair distance distribution functions *p(r)*. For the approximation of the PDDFs 25 splines discretized into 300 points were split non-equidistantly with 10 splines up to 10 nm and the remaining 15 splines covering the range up to *r* = 55 nm. For stabilisation the Lagrange multipliers were varied in the range from 10^{10} down to 10^{-5} in steps of 10^1 and the best Lagrange multipliers were chosen for each scattering curve *I(q)* respectively.

3.3.4 PCG IFT 2D

The 180 scattering curves obtained in *MULIP SAXS 2D* were processed in *PCG IFT 2D* where they provided the basis for the indirect Fourier transformation in two dimensions. For the IFT of the scattering pattern made up of the 180 radial integrations a set of basis functions with 36 splines in azimuthal and 20 splines in radial direction was used whereas the radial direction was discretized into 100 points and the azimuthal one into 4 points per spline. The radial splines were split in a non-uniform way with 10 of these splines in the range r < 10 nm and the remaining radial splines covered the range up to r = 50 nm. Lagrange multiplier variation was done in the range from 10^4 down to 10^0 for the azimuthal stabilisation as well as from 10^2 down to 10^{-2} for the radial stabilisation in steps of $10^{0.5}$ ($\sim$ 3.16) for each direction. Ultimately the following Lagrange multipliers were chosen for processing of all scattering data as they generally seemed to yield the best results.

Table 1: Lagrange multipliers chosen for the stabilisation of the IFT

Lagrange multiplier for radial stabilisation	Lagrange multiplier for azimuthal stabilisation
$\lambda_R = 10^0$	$\lambda_A = 10^{2.5}$

In this way the two-dimensional real space functions, namely the pair distance distribution function *p(r)* as well as the autocorrelation function *γ(r)*, were obtained from the 2D indirect Fourier transformation as well as the approximated scattering patterns in two dimensions.

3.3.5 PCG Viewer 2D

Lastly the two-dimensional PDDFs obtained in *PCG IFT 2D* were cut along and perpendicular to the orientations of the axes (if present) in *PCG Viewer 2D*.

4. Results

4.1   UV-vis spectroscopy

The transmittance spectra of the neat CNC and the CNC/PEG composite films are shown in **Figure 13a** and predominantly a red shift of the reflectance peaks can be seen with increasing PEG content which is confirmed by the corresponding photographs under white light illumination which are depicted in **Figure 13b** showing a slight shift towards green.

a)
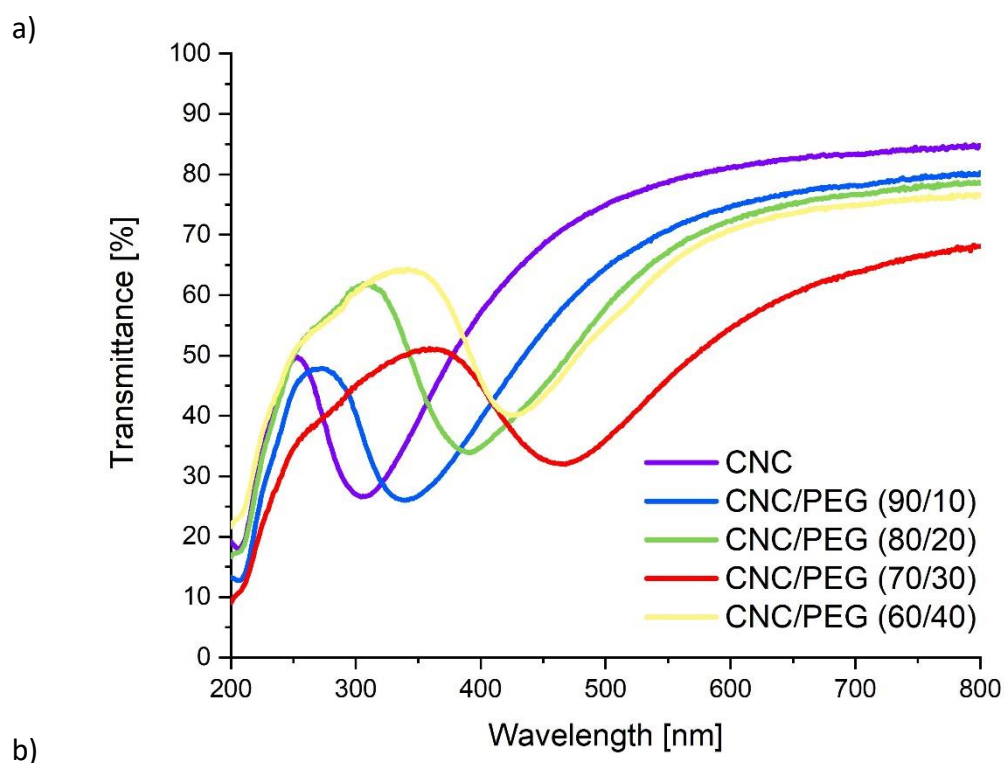
b)
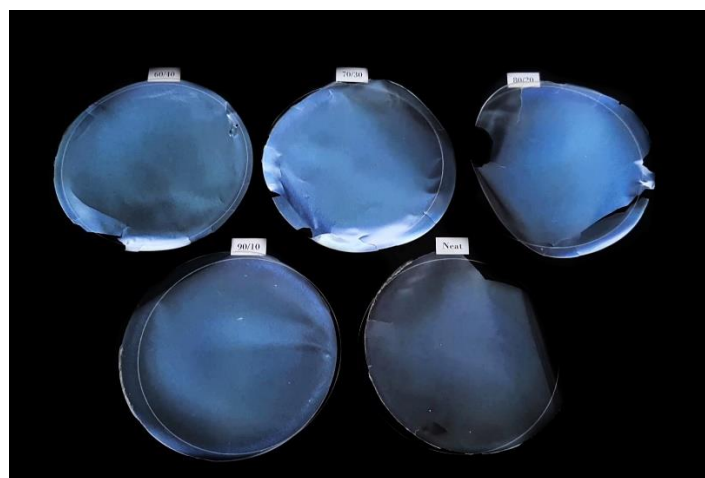
Figure 13: (a) Comparison of the reflection spectra of neat CNC and CNC/PEG composite films showing the range of the reflection peaks over the entire visible spectrum and into the ultraviolet. **(b)** Photographs of the whole series of CNC/PEG composite films with a diameter of 9 cm including the neat CNC film. All photographs were taken in white light.

4.2   Small angle x-ray scattering

4.2.1   Data obtained from reciprocal space

As already mentioned, the scattering patterns (intensity I) obtained in SAXS experiments are usually plotted as a function of the scattering vector q and thus data from reciprocal space is readily available after detection of the scattering patterns. In **Figure 14** the evolution of the detected two-dimensional scattering patterns measured at different angles can be seen for three CNC/PEG composite films whereas the transition from isotropic to anisotropic scattering at larger angles is quite distinct.
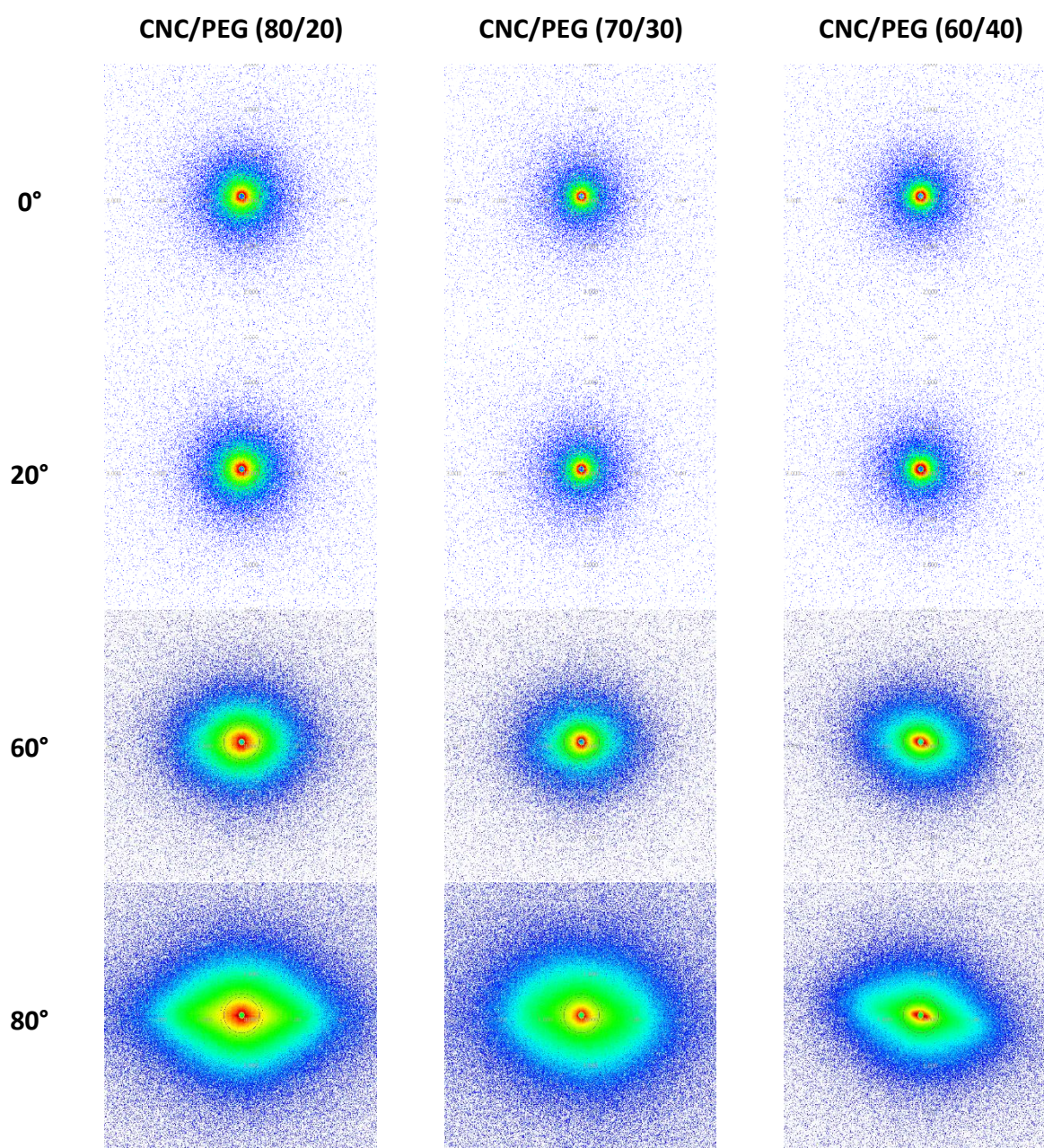
Figure 14: The evolution of the scattering patterns measured at various angles from 0° to 80° for three CNC/PEG composite films, namely CNC/PEG (80/20), CNC/PEG (70/30) and CNC/PEG (60/40) showing the gradual change of the scattering with larger angles.

For the consecutive evaluation of the scattering data by the indirect Fourier transformation in two dimensions 180 scattering curves were obtained from every scattering pattern (see i.a. **Figure 14**) between 0° and 180° by radial integration.

In addition, scattering curves measured at 0° to the primary beam direction were obtained as well by radially integrating the scattering patterns from 0° to 360°. Subsequently these scattering curves were then normalized and averaged as representatively shown in **Figure 15** for the CNC/PEG (80/20) composite film and eventually used for the evaluation of the scattering data by the one-dimensional IFT.
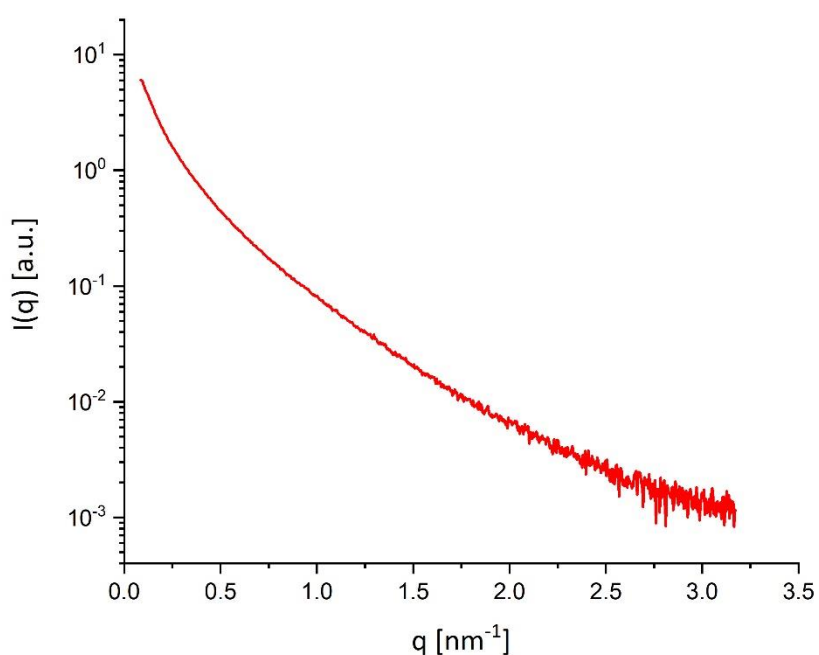
Figure 15: The averaged scattering curve of the CNC/PEG (80/20) composite film measured at 0° to the primary beam direction and further used for the one-dimensional indirect Fourier transformation of the scattering pattern.

4.2.2   Data obtained from real space

Based on the 180 scattering curves the indirect Fourier transformation in two dimensions was carried out yielding real space functions like the two-dimensional pair distance distribution function *p(r)* as well as the two-dimensional autocorrelation function *γ(r)*. For the characterization of the chiral nematic structure of the CNC/PEG composite films *γ(r)* in two dimensions was examined as seen for three CNC/PEG composite films in **Figure 16**.
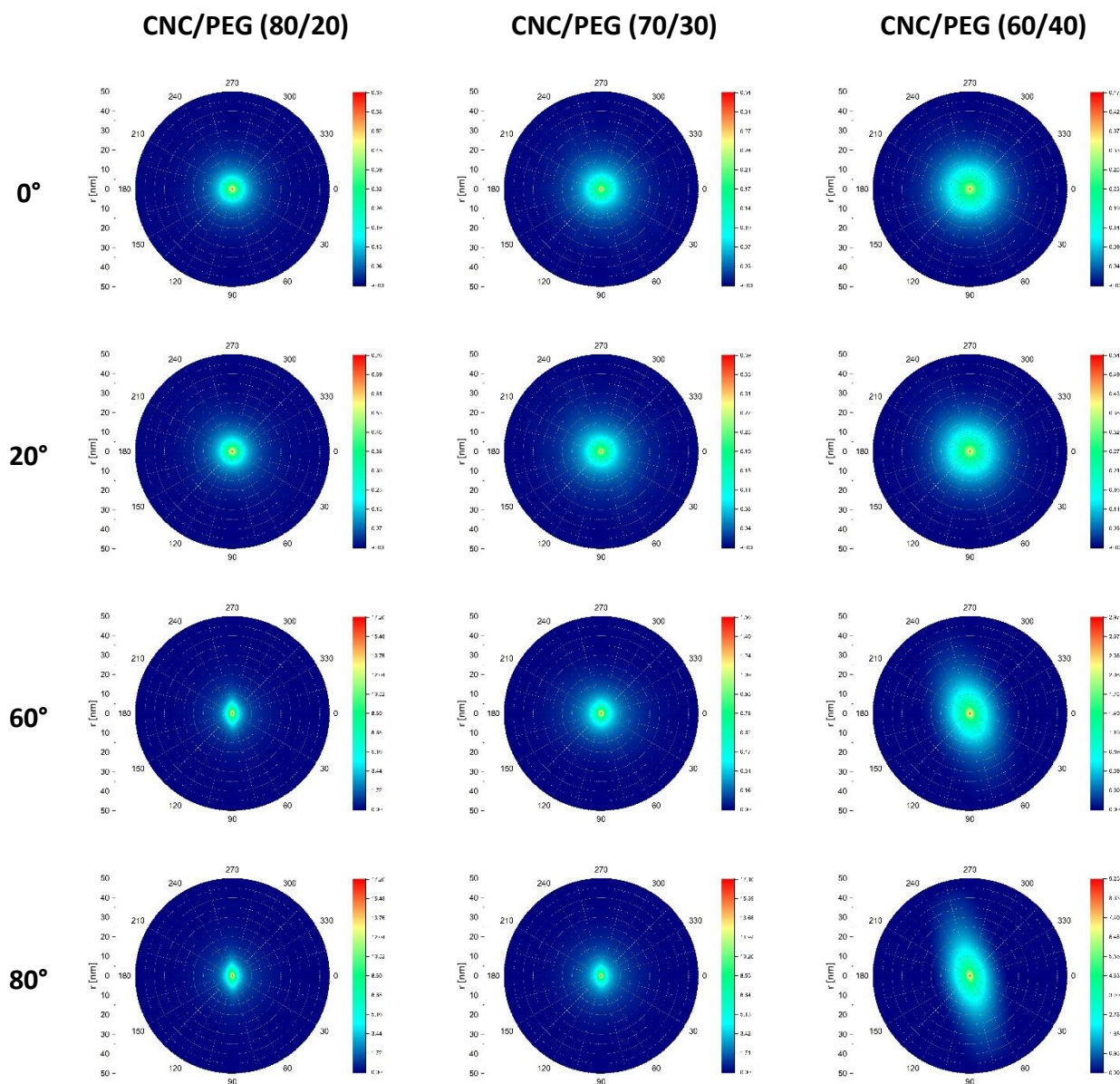
Figure 16: The evolution of the autocorrelation function *γ(r)* computed at various angles from 0° to 80° for three CNC/PEG composite films, namely CNC/PEG (80/20), CNC/PEG (70/30) and CNC/PEG (60/40) showing the gradual change of the "probability of finding oneself in the structure" with larger angles. The corresponding scattering patterns are shown in **Figure 14**.

To gain further information on the nanostructure of the CNC/PEG composite films the two-dimensional PDDFs were cut along as well as perpendicular to the orientations of the axes of the PDDFs yielding one-dimensional pair distance distribution functions. As can be seen in **Figure 16** this was only feasible at larger angles though as the correlation functions and as a consequence the PDDFs were mostly isotropic at lower angles exhibiting no preferential orientation. Therefore, only the PDDF cuts at larger angles are shown in **Figure 17** of all four CNC/PEG composite films with χ denoting the angle to the orientation of the long axis.
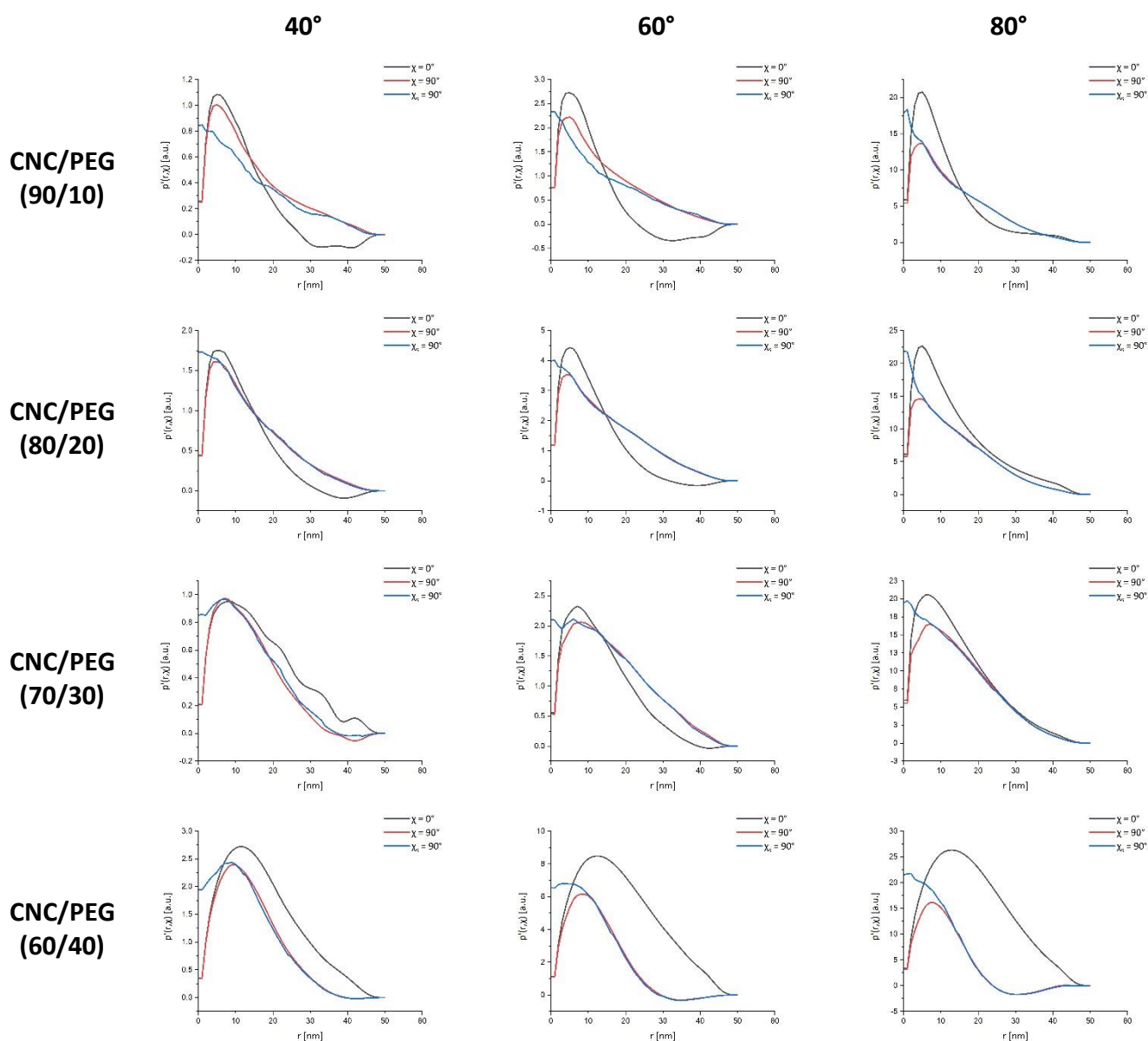
Figure 17: Cuts through the two-dimensional pair distance distribution functions along and perpendicular to the orientations of the present axes of the 2D PDDFs for four CNC/PEG composite films, namely CNC/PEG (90/10), CNC/PEG (80/20), CNC/PEG (70/30) and CNC/PEG (60/40) revealing structural details of the CNC/PEG composite films. The angle to the present axes is denoted by χ whereas χ_S refers to a cut shifted relative to the centre.

To understand the negative values of the PDDFs in **Figure 17** it has to be kept in mind that the PDDFs are histograms of connections weighted by the product of the electron density differences to the mean electron density at the two end-points. Negative contributions to the PDDFs therefore are no mere artefacts and rather correspond to many distances from areas with a positive electron density difference (e.g. cellulose) to areas with a negative electron density difference (e.g. polyethylene glycol). This effect is most pronounced close to a 50/50 volume distribution, since then the mean electron density will be right in between the two electron densities of the components.

It is worth mentioning that the SAXS results of the neat CNC film (100/0) were not included in the analysis as the purely crystalline CNC film did not exhibit any of the characteristics of the other films and could therefore not be compared with any CNC/PEG composites as it didn't contain any polyethylene glycol to begin with.

5. Discussion

5.1 Interpretation of the UV-vis spectrum

As can be clearly seen in **Figure 13a** the reflectance peaks of the CNC/PEG composite films shift from ~307 nm in the ultraviolet to longer wavelengths to ~ 467 nm in the visible spectrum (blue/green) with an increasing PEG content from 0 to 30 wt% supporting the assumption that polyethylene glycol is intercalated between the cellulose nanocrystals leading to an increase in pitch size. The CNC/PEG (60/40) film on the other hand does not fit into this trend and exhibits a blue shift compared to the CNC/PEG (70/30) film due to the crystallisation of PEG which effectively leads to a lower amount of PEG available for intercalation. [7] The synthesis of the CNC/PEG composites with the resulting structural arrangement of CNC and PEG due to the self-assembly of the CNCs is schematically illustrated in **Figure 18** wherein $\frac{P}{2}$ denotes half of the helical pitch.
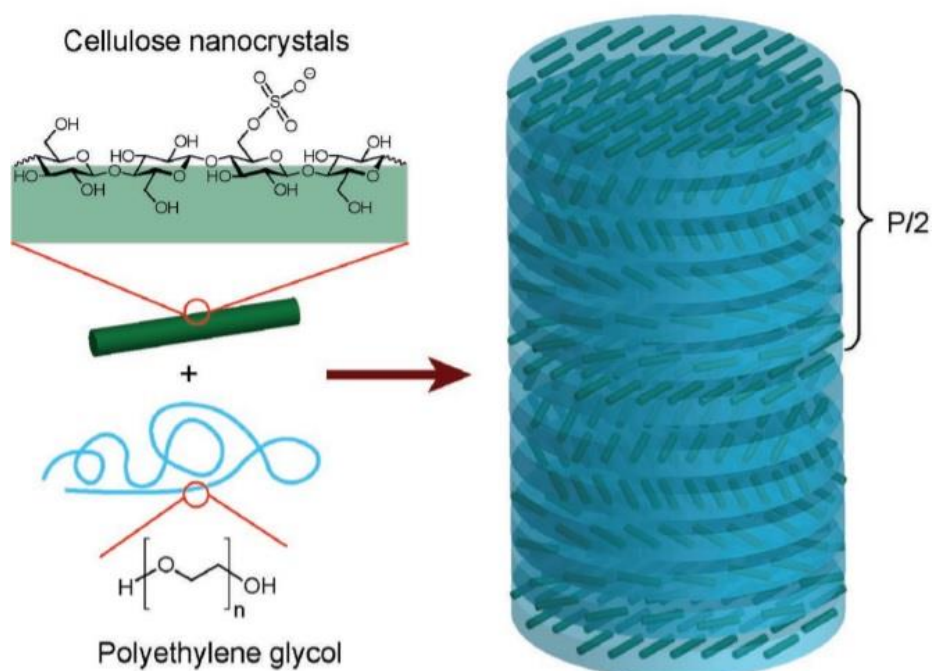
Figure 18: Schematic representation of the synthesis of the CNC/PEG composites displaying a chiral nematic (cholesteric) structure responsible for the photonic properties of the CNC/PEG composite films. CNCs are represented by the green rods while the PEG makes up the light blue matrix. [7]

To verify the assumed nanostructure as given in **Figure 18** one-dimensional as well as two-dimensional real space functions obtained via an indirect Fourier transformation were consulted.

5.2 Evaluation of the IFT results

5.2.1 One-dimensional pair distance distribution functions *p(r)*

In order to confirm the nematic ordering of the cellulose nanocrystals in layers as depicted in **Figure 18** the one-dimensional PDDFs measured at 0° to the primary beam were compared with simulations as shown in **Figure 19** for the CNC/PEG (60/40) composite film.

a)   b)
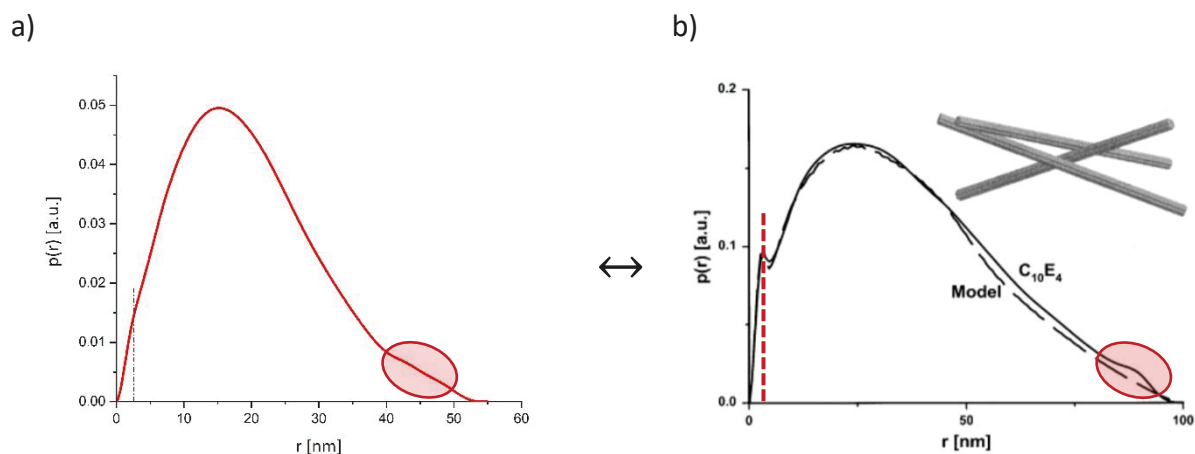
Figure 19: (a) The one-dimensional PDDF of the CNC/PEG (60/40) composite film obtained by radial integration from 0° to 360° of the corresponding isotropic scattering pattern measured at 0° to the primary beam. **(b)** Simulation of the PDDF of two or three cylinders adjacent to each other with similar orientation averaged from a hundred different configurations of two (65%) or three (35%) cylinders. [33]

While the PDDF of a single cylinder typically displays a characteristic overshooting peak at small *r* (see **Figure 7**) the PDDF of multiple cylinders located next to each other with similar tilt is rather blown up at smaller distances as can be seen in **Figure 19b**. [33] Thus treating the cellulose nanocrystals as cylinders and assuming a nematic ordering of the CNCs the behaviour of the PDDF depicted in **Figure 19a** can be interpreted in an analogous way to the simulation. The interpretation is supported by comparing the characteristic features of the measured and simulated PDDF in **Figure 19a** and **Figure 19b** respectively as both for example display a shoulder at lower *r* containing information about the diameter of the cylinders (CNCs). As the position of the shoulder is around $\sim$ 2-3 nm as indicated by the vertical line in **Figure 19a** the diameter of the cellulose nanocrystals can roughly be estimated to be around 3.5-5 nm which is in accordance with the expected size of the CNCs of a few nanometres (5-7 nm) under the used hydrolysis conditions. [7] [22] Next to the similar overall shape of the PDDFs another feature the measured and the simulated PDDFs have in common is the flat peak located at larger *r* further confirming the nematic ordering of the CNCs in layers in the CNC/PEG composites.

5.2.2 Two-dimensional correlation functions γ(r,χ)

From the investigation of the two-dimensional correlation functions as depicted in **Figure 16** it can be seen that γ(r,χ) and consequently the probability of being located in the CNC/PEG nanostructure is getting more anisotropic with larger angles in all samples. This can be understood by treating the helicoidal structure of the CNC/PEG composite films given in **Figure 18** as lamellar. This means that at larger angles to the director the beam only illuminates part of the helicoidal structure, namely a layer of the cholesteric structure, while additionally cellulose nanocrystals parallel to the beam vanish. The broadening of the correlation function along a direction with higher angles can therefore simply be interpreted as looking at the helicoidal structure from the side and illuminating a CNC/PEG layer of the cholesteric structure. The orientation of the anisotropic γ(r,χ) then corresponds to the orientation of the illuminated layer with γ(r,χ) representing a projection of the layer thickness. For a better understanding this is visualized in **Figure 20** for the CNC/PEG (60/40) composite film.
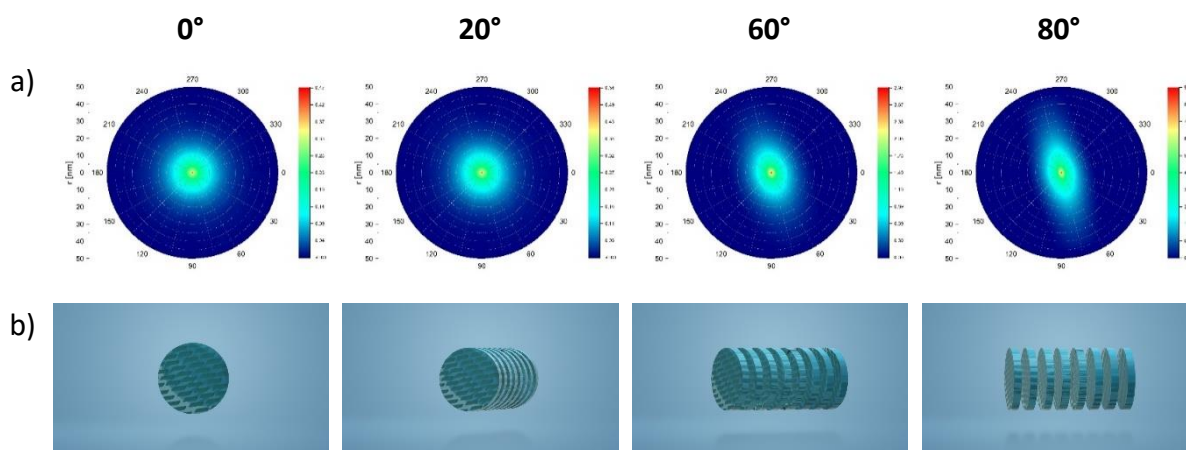
Figure 20: The two-dimensional autocorrelation functions **(a)** with the corresponding views on the chiral nematic structure **(b)** of the CNC/PEG (60/40) composite film at different angles. For better visualisation, the different CNC/PEG layers of the chiral nematic structure are shown separately in **(b)**.

5.2.3 One-dimensional correlation functions γ'(r,χ)

By cutting the anisotropic 2D correlation functions perpendicularly to the long axes the dimensions of the single layers could be qualitatively determined and even neighbouring layers could be distinguished as seen in **Figure 21a** by the slight increase of γ'(r,χ) around ± 45 nm for the CNC/PEG (60/40) at 80° to the primary beam.

Further information about the dimensions of the next layer could not be extracted from the one-dimensional correlation functions as the resolution was limited to the maximum $D_{max} \sim 50$ nm at a SDD of 675 mm according to the sampling theorem of the Fourier transformation which is given in the following. [10] [15]

$$D_{max} \approx \frac{\pi}{q_{min}} \qquad (26)$$

Comparing the one-dimensional correlation functions obtained from the CNC/PEG (60/40) composite film at 80° with the one-dimensional $\gamma(r)$ of the ideal lamellar model after Vonk and Kortleve [34] further supports the arrangement of the CNC and PEG in layers. The corresponding correlation functions calculated for different distribution functions of the thicknesses of the crystalline and amorphous layers are shown in **Figure 21b** whereas curve c is most similar to the one of CNC/PEG (60/40) at 80° indicating a broad distribution of the crystalline and amorphous layers in the CNC/PEG composites. Treating the CNC/PEG nanostructure hence as a lamellar structure the layer thickness could be estimated to be ~ 10 nm and the distance to the next layer ~ 45 nm for the CNC/PEG 60/40 composite film.
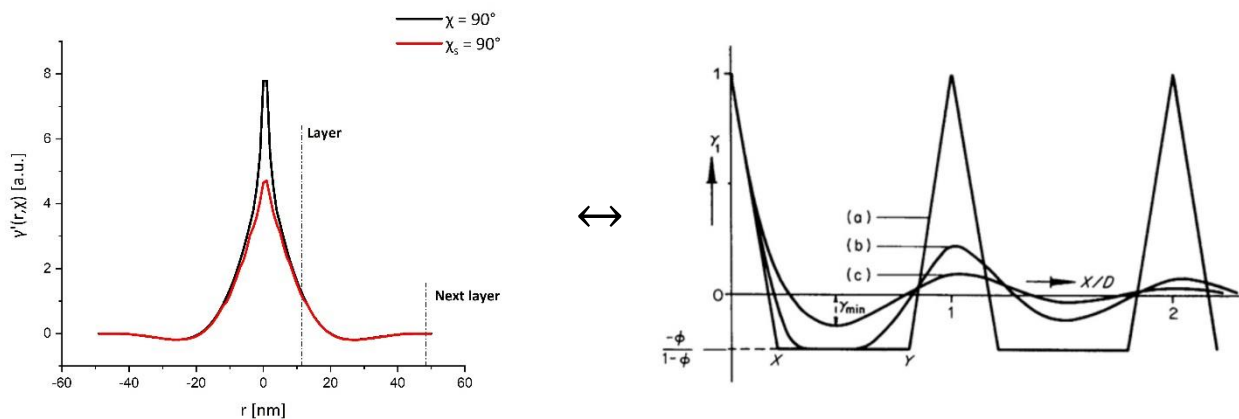
Figure 21: (a) One dimensional autocorrelation functions obtained by cutting the 2D $\gamma(r, \chi)$ of the CNC/PEG (60/40) composite film measured at 80°. The angle to the present axes is denoted by χ whereas χ_S refers to a cut shifted relative to the centre. **(b)** One-dimensional autocorrelation functions according to the ideal lamellar model for three different widths of the thickness distribution functions of the crystalline and amorphous layers with curves (a) to (c) referring to increasing widths of the distributions. [15]

To verify the arrangement of the CNCs in layers indicating a chiral nematic ordering the two-dimensional $\gamma(r,\chi)$ were cut another time perpendicularly but shifted relative to the centre up to ± 15 nm which is illustrated in **Figure 21a** by the red line labelled χ_S. As can be seen this led to the same one-dimensional $\gamma'(r, \chi)$ as beforehand as expected for the nematic ordering of the CNCs in the layers. After all the thickness of the layers should stay constant and therefore yield the same one-dimensional $\gamma'(r, \chi)$ along the layer.

5.3   Impact of increasing polyethylene glycol content

In a similar fashion the shift of spacing between the layers with an increasing amount of PEG was investigated by looking at the cuts perpendicular to the long axes of the two-dimensional pair distance distribution functions $p'(r,\chi)$ measured at 60° to the primary beam as shown in the following in **Figure 22**.
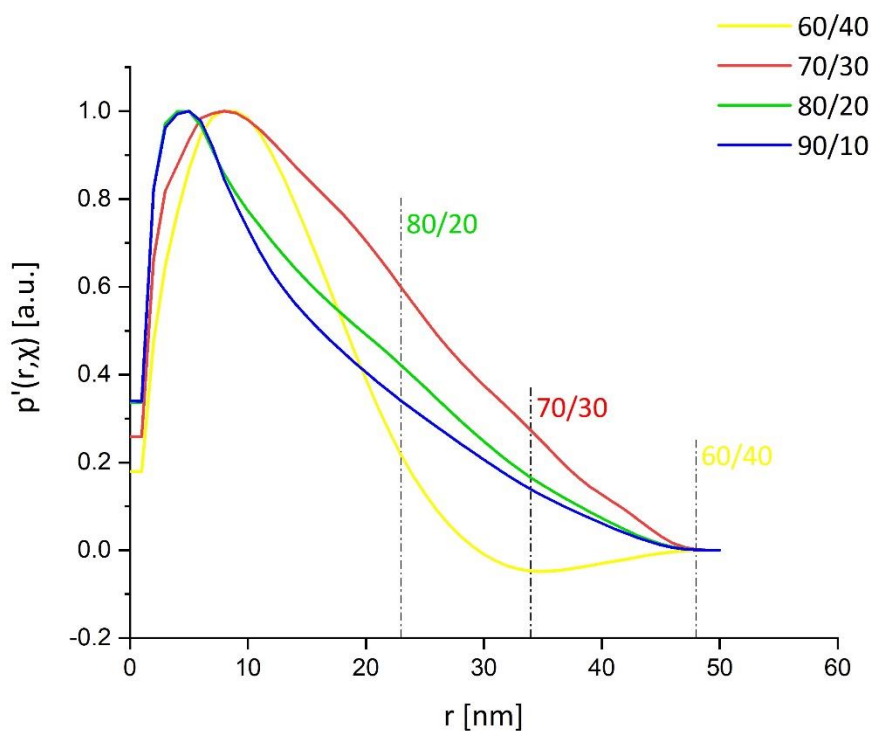
Figure 22: Comparison of the one-dimensional PDDFs $p'(r,\chi)$ perpendicular to the long axes of the corresponding 2D PDDFs of the whole series of CNC/PEG composite films. A clear trend towards larger distances between the layers with increasing PEG content is evident and the accompanying shift of the shoulder of the PDDFs with higher amounts of PEG is indicated by the vertical lines.

A trend towards larger spacing between the layers from ∼ 23 nm for the CNC/PEG (80/20) composite film to ∼ 48 nm for the CNC/PEG (60/40) composite film can be seen with increasing PEG content in **Figure 22** as the shoulder of the PDDF corresponding to the neighbouring layer moves to larger r indicated by the vertical lines for the different amounts of PEG in **Figure 22**. First visible as the overshooting peak of the CNC/PEG (90/10) at smaller r the peak slowly shifts into the peak located around 50 nm of the CNC/PEG (60/40) composite film confirming the intercalating effect of PEG leading to greater spacing between the layers.

5.4   Investigation of the influence of humidity

To better understand the influence of humidity on the CNC/PEG nanostructure, tests at elevated relative humidity levels were performed. For this a sample-to-detector distance of 1052 mm compared to the previously used SDD of 675 mm was chosen yielding a comparably higher resolution of up to 80 nm to obtain a better overview of the structural changes of the CNC/PEG nanostructure in response to humidity. Due to polyethylene glycols hygroscopic nature an increase in humidity lead to swelling of the chiral nematic structure and subsequent increase in layer spacing. This can be seen in **Figure 23** in which the one-dimensional PDDFs of the CNC/PEG (60/40) at 60° in the dry state and the humid state are compared.
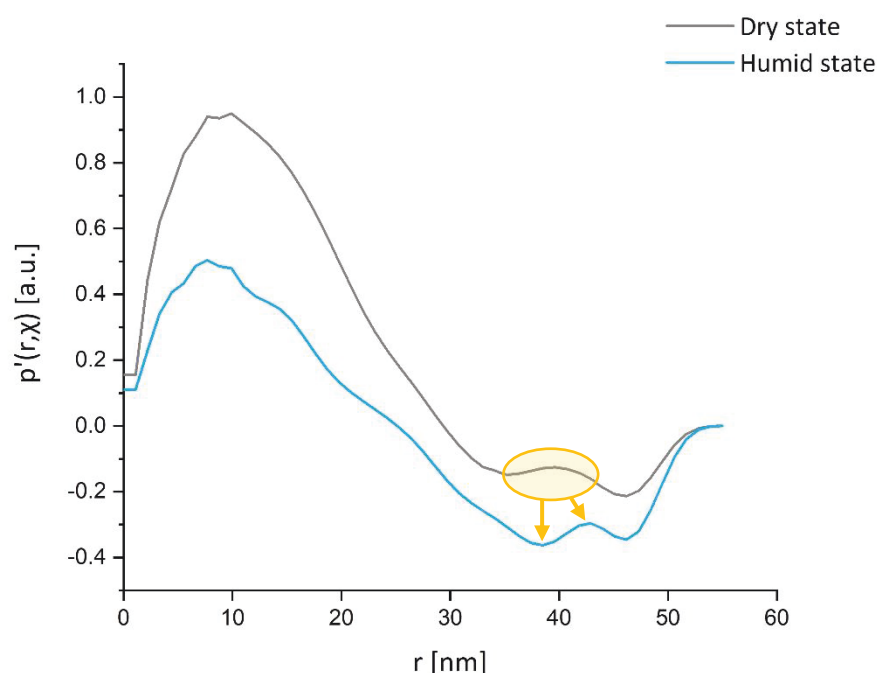
Figure 23: Comparison of the one-dimensional pair distance distribution functions of the CNC/PEG (60/40) composite film at 60° in the dry and in the humid state showing the shift of the PDDFs' minima as well as the displacement of the peak corresponding to the neighbouring layer to larger distances. The 1D PDDFs were obtained by cutting the two-dimensional PDDFs perpendicularly to the long axes.

In order to understand this change of the PDDF in response to humidity the previously introduced ideal lamellar model after Vonk and Kortleve can be used again for interpretation: As shown in **Figure 21b** the size of the minimum is proportional to the volume content of the smaller phase, PEG in the case of the CNC/PEG composites, meaning that an increase in said phase will consequently also yield a more pronounced minimum. As polyethylene glycol is mainly taking up the water thereby increasing its volume content in the overall nanostructure the change of the PDDFs minima can therefore be ascribed to the water uptake of PEG as indicated by the downward facing arrow in **Figure 23**.

The cellulose nanocrystals on the other hand remain unaltered due to their resistance to water penetration [35] and thus the water absorption solely effects PEG leading to the observed colour change of the CNC/PEG composite films confirming the intercalation of PEG between the CNCs. This intercalating effect of PEG is further supported by the displacement of the peak corresponding to the neighbouring layer to larger distances as indicated by the rightward pointing arrow in **Figure 23**.

6. Conclusion

In the present thesis nanocellulose based composite films with different amounts of polyethylene glycol ranging from 0 to 40 wt% were synthesized at the KTH Royal Institute of Technology in Stockholm, Sweden and then further investigated by small angle x-ray scattering at the Montanuniversität Leoben in Austria.

The main objective of this thesis was to obtain a better understanding of the photonic structure of the CNC/PEG composites depending on the polyethylene glycol content or more specifically how the PEG integration into the chiral nematic structure of the CNCs takes place affecting the consequent photonic properties. For this purpose, a series of CNC/PEG composite films with weight ratios of CNC and PEG varying from 100/0 to 60/40 were synthesized and then investigated by small angle x-ray scattering at different angles to the primary beam. The analysis of the scattering data in the form of a one-dimensional indirect Fourier transformation already confirmed the nematic ordering of the cellulose nanocrystals in layers when comparing the measured PDDFs with simulations.

From the subsequent evaluation of the scattering data in the form of a two-dimensional indirect Fourier transformation other structural parameters could be qualitatively extracted as well. It could be shown that by assuming an ideal lamellar model for the CNC/PEG composites information about the nanostructure could be obtained directly from real space functions like the pair distance distribution function $p(r,\chi)$ as well as the radial autocorrelation function $\gamma(r,\chi)$. In this way the change in layer spacing with corresponding PEG contents could be qualitatively determined as shown in **Figure 24** in accordance with the macroscopically visible structural colour change with varying amounts of PEG. As the nematic layers were illuminated by the x-ray beam at an angle the layer spacing shown in **Figure 24** was corrected accounting for the respective viewing angle.
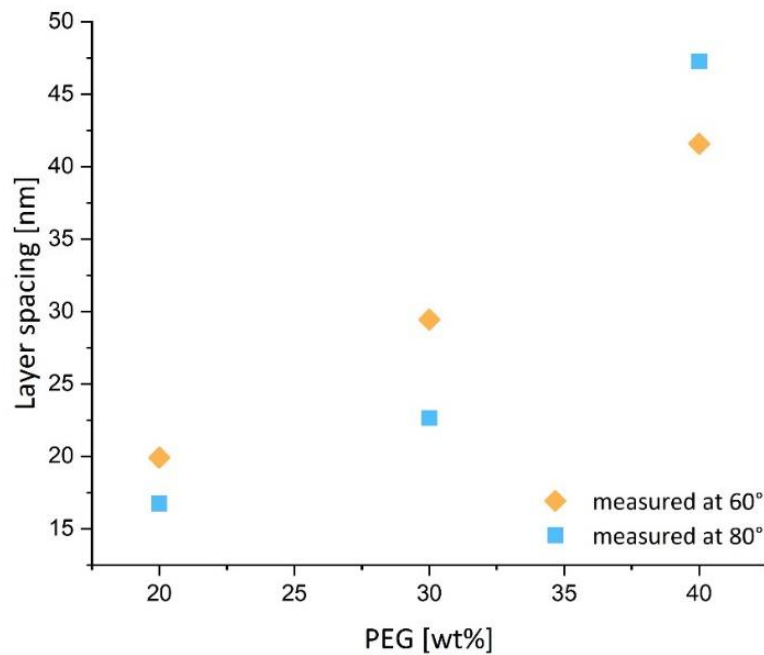
Figure 24: Angle-corrected layer spacing as a function of the polyethylene glycol content shown for two different angles to the primary beam. It has to be noted that only measurements at higher angles to the primary beam were taken into account as then the layer spacing was best visible.

Consistent with the ideal lamellar model the characteristic swelling of the chiral nematic structure of the CNC/PEG composite films at elevated relative humidity levels could be identified as well by looking at the one-dimensional cuts through the two-dimensional real space functions indicating an increase of the volume content of PEG with water uptake.

Complementing this qualitative analysis, GISAXS in transmission mode [36] on a smooth substrate at the synchrotron as well as the modification of the parameters of the IFT might improve the qualitative analysis of the nanostructure of the CNC/PEG composites given here.

In summary, the combination of small angle x-ray scattering with the two-dimensional indirect Fourier transformation has proven to be a very powerful tool in analysing nanostructured composites even as complex as the CNC/PEG composite films synthesized in this thesis.

7. References

[1]   Mishnaevsky, L., & Tsapatsis, M. (2016). Hierarchical materials: Background perspectives. *MRS Bulletin*, *41*(9), 661–664. https://doi.org/10.1557/mrs.2016

[2]   Lakes, R. (1993). Materials with structural hierarchy. *Nature*, *361*(6412), 511–515. https://doi.org/10.1038/361511a0

[3]   Fratzl, P., & Weinkamer, R. (2007). Nature's hierarchical materials. *Progress in Materials Science*, *52*(8), 1263–1334. https://doi.org/10.1016/j.pmatsci.2007.06.001

[4]   Kannarath, A. (2014). *Mimicking Nature: A Solution for Sustainable Development*. Partridge Publishing India. https://books.google.at/books?id=U9IAAwAAQBAJ

[5]   Revol, J. F., Bradford, H., Giasson, J., Marchessault, R. H., & Gray, D. G. (1992). Helicoidal self-ordering of cellulose microfibrils in aqueous suspension. *International Journal of Biological Macromolecules*, *14*(3), 170–172. https://doi.org/10.1016/S0141-8130(05)80008-X

[6]   Ohm, W., Rothkirch, A., Pandit, P., Körstgens, V., Müller-Buschbaum, P., Rojas, R., Yu, S., Brett, C. J., Söderberg, D. L., & Roth, S. V. (2018). Morphological properties of airbrush spray-deposited enzymatic cellulose thin films. *Journal of Coatings Technology and Research*, *15*(4), 759–769. https://doi.org/10.1007/s11998-018-0089-9

[7]   Yao, K., Meng, Q., Bulone, V., & Zhou, Q. (2017). Flexible and Responsive Chiral Nematic Cellulose Nanocrystal/Poly(ethylene glycol) Composite Films with Uniform and Tunable Structural Color. *Advanced Materials*, *29*(28), 1–8. https://doi.org/10.1002/adma.201701323

[8]   Parker, R. M., Guidetti, G., Williams, C. A., Zhao, T., Narkevicius, A., Vignolini, S., & Frka-Petesic, B. (2018). The Self-Assembly of Cellulose Nanocrystals: Hierarchical Design of Visual Appearance. *Advanced Materials*, *30*(19). https://doi.org/10.1002/adma.201704477

[9]   Gray, D. G. (2016). Recent advances in chiral nematic structure and iridescent color of cellulose nanocrystal films. *Nanomaterials*, *6*(11). https://doi.org/10.3390/nano6110213

[10]   Schnablegger, H., & Singh, Y. (2013). The SAXS Guide. *Anton Paar GmbH*, 1–99. https://doi.org/10.1006/aphy.1994.1055

[11]   Prehal, C. (2014). "*In-situ SAXS study on the ion dynamics in microporous carbon based supercapacitors.*", Diploma Thesis, Montanuniversität Leoben

[12]   Als-Nielsen, J., & McMorrow, D. (2011). Elements of Modern X-ray Physics: Second Edition. In *Elements of Modern X-ray Physics: Second Edition*. https://doi.org/10.1002/9781119998365

[13]   Feigin, L. A., & Svergun, D. I. (1987). Structure Analysis by Small-Angle X-Ray and Neutron Scattering. In *Structure Analysis by Small-Angle X-Ray and Neutron Scattering*. https://doi.org/10.1007/978-1-4757-6624-0

[14]   Sharma, S. K., Verma, D. S., Khan, L. U., Kumar, S., & Khan, S. B. (2018). Handbook of Materials Characterization. In *Handbook of Materials Characterization*. https://doi.org/10.1007/978-3-319-92955-2

[15]   O. Glatter and O. Kratky, SMALL ANGLE X-RAY SCATTERING. London: Wiley, 1982.

[16]   Paris, O. MUL lecture manuscript, Introduction into Synchrotron Radiation. 2019.

[17]   Debye, P. (1915). Zerstreuung von Röntgenstrahlen. *Annalen Der Physik*, *351*(6), 809–823. https://doi.org/10.1002/andp.19153510606

[18]   T. Narayanan, Soft Matter Characterization. (2008). In *Soft Matter Characterization*. https://doi.org/10.1007/978-1-4020-4465-6

[19]   Glatter, O. (1977). A new method for the evaluation of small-angle scattering data. *Journal of Applied Crystallography*, *10*(5), 415–421. https://doi.org/10.1107/s0021889877013879

[20]   Mittelbach, P. & Porod, G. Zur Röntgenkleinwinkelstreuung verdünnter kolloidaler Systeme VII. Die Berechnung der Streukurven von dreiachsigen Ellipsoiden. Acta Phys. Aust., 1962, XV, 122-147

[21]   Fritz, G., & Glatter, O. (2006). Structure and interaction in dense colloidal systems: Evaluation of scattering data by the generalized indirect Fourier transformation method. *Journal of Physics Condensed Matter*, *18*(36), 2403–2419. https://doi.org/10.1088/0953-8984/18/36/S14

[22]   Glatter, O. (1979). The interpretation of real-space information from small-angle scattering experiments. *Journal of Applied Crystallography*, *12*(2), 166–175. https://doi.org/10.1107/s0021889879012139

[23]   Fritz-Popovski, G. (2013). Two-dimensional indirect Fourier transformation for evaluation of small-angle scattering data of oriented samples. *Journal of Applied Crystallography*, *46*(5), 1447–1454. https://doi.org/10.1107/S002188981302150X

[24]   Fritz-Popovski, G. (2015). Interpretation of two-dimensional real-space functions obtained from small-angle scattering data of oriented microstructures. *Journal of Applied Crystallography*, *48*(1), 44–51. https://doi.org/10.1107/S1600576714024972

[25]   Guinier, A., Fournet, G., & Walker, C. B. (1955). *SCATTERING OF X-RAYS*.

[26]   Svergun, D. I., Semenyuk, A. V., & Feigin, L. A. (1988). Small-angle-scattering-data treatment by the regularization method. *Acta Crystallographica Section A*, *44*(3), 244–251. https://doi.org/10.1107/S0108767387011255

[27]   Beck-Candanedo, S., Roman, M., & Gray, D. G. (2005). Effect of reaction conditions on the properties and behavior of wood cellulose nanocrystal suspensions. *Biomacromolecules*, *6*(2), 1048–1054. https://doi.org/10.1021/bm049300p

[28]   Zhou, Q., Brumer, H., & Teeri, T. T. (2009). Self-organization of cellulose nanocrystals adsorbed with xyloglucan oligosaccharide-poly (ethylene glycol)-polystyrene triblock copolymer. *Macromolecules*, *42*(15), 5430–5432. https://doi.org/10.1021/ma901175j

[29]   Grewer, T., & Rogers, R. L. (1993). Exothermic secondary reactions. *Thermochimica Acta*, *225*(2), 289–301. https://doi.org/10.1016/0040-6031(93)80195-G

[30]   Huang, T. C., Toraya, H., Blanton, T. N., & Wu, Y. (1993). X-ray powder diffraction analysis of silver behenate, a possible low-angle diffraction standard. *Journal of Applied Crystallography*, *26*(pt 2), 180–184. https://doi.org/10.1107/S0021889892009762

[31]   Brumberger, H. (1995). *Modern aspects of small-angle scattering.* Dordrecht: Kluwer.

[32]   Zhang, F., Ilavsky, J., Long, G. G., Quintana, J. P. G., Allen, A. J., & Jemian, P. R. (2010). Glassy carbon as an absolute intensity calibration standard for small-angle scattering. *Metallurgical and Materials Transactions A: Physical Metallurgy and Materials Science*, *41*(5), 1151–1158. https://doi.org/10.1007/s11661-009-9950-x

[33]   Glatter, O., Fritz, G., Lindner, H., Brunner-Popela, J., Mittelbach, R., Strey, R., & Egelhaaf, S. U. (2000). Nonionic micelles near the critical point: Micellar growth and attractive interaction. Langmuir, 16(23), 8692–8701. https://doi.org/10.1021/la000315s

[34]   Vonk, C.G., Kortleve, G. X-ray small-angle scattering of bulk polyethylene. Kolloid-Z.u.Z.Polymere 220, 19–24 (1967). https://doi.org/10.1007/BF02086052

[35]   Lahiji, R. R., Xu, X., Reifenberger, R., Raman, A., Rudie, A., & Moon, R. J. (2010). Atomic force microscopy characterization of cellulose nanocrystals. *Langmuir*, *26*(6), 4480–4488. https://doi.org/10.1021/la903111j

[36]   Lu, X.; Yager, K. G.; Johnston, D.; Black, C. T. & Ocko, B. M. Grazing-incidence transmission X-ray scattering: surface scattering in the Born approximation. Journal of Applied Crystallography, 2013, 46, 165-172